Post-embryonic development and aging of the appendicular skeleton in *Ambystoma mexicanum*

Camilo Riquelme-Guzmán[1], Maritta Schuez[1], Alexander Böhm[1], Dunja Knapp[1], Sandra Edwards-Jorquera[1], Alberto S. Ceccarelli[2], Osvaldo Chara[2,3,4], Martina Rauner[5,6], Tatiana Sandoval-Guzmán[1,6]

[1]Technische Universität Dresden, CRTD/ Center for Regenerative Therapies TU Dresden, Dresden, Germany.
[2]System Biology Group (SysBio), Institute of Physics of Liquids and Biological Systems (IFLySiB), National Scientific and Technical Research Council (CONICET) and University of La Plata, La Plata, Argentina.
[3]Instituto de Tecnología, Universidad Argentina de la Empresa (UADE), Buenos Aires, Argentina.
[4]Center for Information Services and High Performance Computing (ZIH), Technische Universität Dresden, Dresden, Germany.
[5]Department of Medicine III, Universitätsklinikum Dresden, Dresden, Germany.
[6]Center for Healthy Aging, Universitätsklinikum Dresden, Dresden, Germany.

Correspondence
Tatiana Sandoval-Guzmán, Technische Universität Dresden, CRTD/Center for Regenerative Therapies TU Dresden, Dresden Germany
Email: tatiana.sandoval_guzman@tu-dresden.de

Keywords
Axolotl, ossification, aging, chondrocytes, osteoblasts

Abstract

Background

The axolotl is a key model to study appendicular regeneration. The limb complexity resembles that of humans in structure and tissue components; however, axolotl limbs develop post-embryonically. In this work, we evaluated the post-embryonic development of the appendicular skeleton and its changes with aging.

Results

The juvenile limb skeleton is formed mostly by *Sox9*/*Col1a2* cartilage cells. Ossification of the appendicular skeleton starts when animals reach a length of 10 cm, and cartilage cells are replaced by a primary ossification center, consisting of cortical bone and an adipocyte-filled marrow cavity. Vascularization is associated with the ossification center and the marrow cavity formation. We identified the contribution of *Col1a2*-descendants to bone and adipocytes. Moreover, ossification progresses with age towards the epiphyses of long bones. Axolotls are neotenic salamanders, and still ossification remains responsive to L-thyroxine, increasing the rate of bone formation.

Conclusions

In axolotls, bone maturation is a continuous process that extends throughout their life. Ossification of the appendicular bones is slow and continues until the complete element is ossified. The cellular components of the appendicular skeleton change accordingly during ossification, creating a heterogenous landscape in each element. The continuous maturation of the bone is accompanied by a continuous body growth.

Introduction

Urodeles are the only vertebrates with the ability to regenerate a whole limb as adults, therefore they offer the unique opportunity to gain important insights to advance regenerative medicine. The axolotl (*Ambystoma mexicanum*) is a gold standard for studying limb regeneration in vertebrates. The progenitor cells in the blastema, a key structure for epimorphic regeneration, are a heterogeneous population that remain restricted to their embryonic origin.[1] Given the cellular heterogeneity of the blastema, the contribution of specific cell populations during regeneration has been the focus of significant research in the last decade. An interesting exception is the skeleton: cells embedded in the skeletal matrix do not participate in regeneration; instead, the skeleton is restored by periskeletal cells and dermal fibroblasts.[2–4]

While mammals are born with partially ossified bones that will conclude postnatally, ossification in most amphibians is coupled with metamorphosis.[5–7] However, axolotls remain neotenic and, hence, they maintain juvenile features throughout life and only rarely undergo metamorphosis. Their adulthood is marked by reaching sexual maturity, a slowing growth rate, and by ossification of the appendicular skeleton.[8,9] The physiological context in which appendicular ossification occurs in axolotls as well as the cellular transitions within the skeleton are unclear. In the anuran amphibian, *Xenopus laevis*, the extent of ossification negatively correlates with the regenerative potential of the limb. During metamorphosis and as bone ossifies, the regenerative capacity declines in the ossifying areas, while amputation at the cartilaginous joints still regenerates.[10] Limb regeneration in salamanders remains a feature of adult animals; however, regeneration also declines with age and after metamorphosis.[11] It remains unclear if the correlation between appendicular ossification and decreased regeneration holds true for the axolotl, and more importantly, if the regeneration mechanisms studied so far are replicated when the cellular and extracellular matrix landscapes change in the skeleton as they age. In this study, we analyzed larvae, adult and aged axolotls to document the transition of the appendicular skeleton from a cartilaginous to ossified skeleton.

In general, appendicular bones develop by endochondral ossification, a process where a cartilage anlage is replaced by bone.[12,13] During development, mesenchymal progenitors

condense and form a cartilage primordium which expands by proliferation of chondrocytes. Cells located in the central diaphysis differentiate into hypertrophic chondrocytes (HCs), which subsequently induce the recruitment of blood vessels, osteoclasts and osteoblasts, giving rise to the primary ossification center. Within the diaphysis, the cartilage matrix is degraded, osteoblasts replace the tissue with cortical bone and a marrow cavity is formed. Simultaneously, osteoblasts located in the perichondrium form a bone collar around the diaphysis and the periosteum is established. Many HCs undergo apoptosis during endochondral ossification; however, several studies have shown a partial contribution from HCs to bone formation through transdifferentiation into osteoblasts.[14–16] Moreover, Giovannone *et al.* showed that HCs can also transdifferentiate into adipocytes in the ceratohyal bone in zebrafish, highlighting the importance and participation of HCs in the ossification process. In axolotls, however, endochondral ossification is a post-embryonic process. Whether it is driven by the hormonal changes of sexual maturity, environmental cues or body mass, is not yet determined.

In this work, we evaluated the post-embryonic development of the appendicular skeleton of axolotls, from larvae to aged adults. We analyzed the morphological and cellular changes in the zeugopodial elements, the radius and ulna, and we identified the timing in which ossification of those elements occurred. Moreover, we examined the cellular landscape of the radius and the possible contribution of chondrocytes to bone formation in ulnas. Finally, we observed in adult and aged animals (5- to 20-years) a continuous ossification in all limb skeletal elements. Hence, our work provides a detailed view of how the appendicular skeleton, particularly the zeugopod, matures from a cartilage anlage towards a bone.

127

128

129 **Results**

130

131 **Axolotls transition from a rapid to a slower growth phase at about 10 months of age.**

132 Few studies include aged animals beyond the well-determined larval stages[17] and the
133 neoteny of the axolotl raises controversy on the limit of its growth. In this study, we used
134 animals grown in fully standardized conditions[18] and we defined their appendicular
135 development in relation to their maturation stage.

136 Using the snout to tail (ST) and snout to vent (SV) lengths, we recorded the size and
137 age in 220 axolotls. ST and SV lengths are highly correlated (Pearson coefficient r = 0.9937, p
138 = 3.1 10^{-209}, Fig. 1A) and their normograms presented a similar trend: a rapid growth phase
139 followed by a slower growth phase (Fig. 1B, 1C, dots). To test whether there is a transition
140 between two subsequent growth modes, we followed a previously reported approach[19,20] to
141 determine the border separating two spatial regions within the anterior-posterior axis of the
142 axolotl spinal cord during regeneration (see methods section). We fitted the ST and SV
143 normograms with a two-line mathematical model, assuming two subsequent linear growths
144 separated by a transition age (Fig. 1B, 1C, continuous line). We estimated the two-line
145 transition age in (a_t^{TL}): 19.87 ± 0.07 and 19.00 ± 0.07 months for ST and SV normograms,
146 respectively (where the errors were estimated by bootstrapping). The slope of the first line
147 (m_1) was higher than the slope of the second line (m_2) for the ST normogram (m_1 = 1.144 ±
148 0.003 cm/month *vs*. m_2 = 0.0325 ± 0.0006 cm/month, no overlapping within three times the
149 errors) as well as for the SV normograms (m_1 = 0.618 ± 0.002 cm/month *vs*. m_2 = 0.0202 ±
150 0.0004 cm/month, no overlapping within three times the errors). Interestingly, the slope of
151 the second line was higher than zero (*i.e*., zero was smaller than the second line slope minus
152 three times its error, both for ST and SV lengths), indicating that after the transition time, the
153 axolotl continues growing.

154 To mechanistically address the descriptive results obtained with the two-line model,
155 we tested whether the normograms could be recapitulated by a linear growth model
156 assuming a time-dependent growth rate (see methods section). In particular, we assumed that
157 the growth rate follows an age-dependent Hill-expression. The model successfully fit both
158 normograms (Fig. 1D, 1E) and allowed us to predict the age-dependent growth rate, a proxy

159 for the global proliferation rate in the axolotl (Fig. 1F, 1G). The model allows us to predict the
160 growth rate for animals of old ages, which resulted in (1/month): 0.00116 ± 0.00003 and
161 0.00142 ± 0.00002 for ST and SV lengths, respectively, both being higher than zero, in
162 agreement with the result obtained with the two-line model. More importantly, we
163 determined two subsequent growth rate regimes separated by the growth rate transition age
164 (a_t^{GR})given by the inflexion point, estimated as 9.87 ± 0.05 and 11.07 ± 0.05 months for the ST
165 and SV lengths, respectively. Hence, our analysis suggests that the two-line transition age of
166 approximately 20 months is an emergent phenomenon resulting from the growth rate
167 transition age of about 10 months.

168 The biological context of this transition relates to animals reaching sexual maturity.
169 We documented animal growth in the context of sexual maturity in our axolotl colony.
170 Remarkably, we found that the first signs of secondary sexual features in males appear around
171 10 months of age, and by 12 months these features are fully developed. However, a successful
172 mating starts only between 11 and 12 months of age. Females develop the first secondary
173 sexual features slightly later than males (between 10-11 months of age) but like males, by 12
174 months these features are fully developed. Fertility is first successful in females between 12-
175 14 months of age. Hence, the agreement between the transition time separating the faster
176 from the following slower growth rate and the age of appearance of the secondary sexual
177 features suggests a probable causal link.

178 Of note, in 1-year-old siblings, ST was significantly longer in males than females (males:
179 20.06 ± 0.6 cm, females: 17.78 ± 0.4 cm, n = 9), while SV remained constant (males: 9.8 ± 0.3
180 cm, females: 9.3 ± 0.3 cm, n = 9) (Fig. 1H). In 2.5-month-old juvenile larvae siblings, ST did not
181 differ (males: 4.7 ± 0.2 cm, females: 4.7 ± 0.2 cm, n = 12). This indicates that the differences
182 in total length between sexes is due to an increased tail growth in males upon sexual
183 maturation.

184

185 **The zeugopodial skeleton is progressively ossified with growth**

186 We evaluated the post-embryonic development of the appendicular skeleton,
187 particularly the long bones from the zeugopod. We used animals ranging from ST 4 to 20 cm,
188 which represent axolotls from a juvenile stage to adulthood. Using alcian blue/alizarin red
189 staining, we first evaluated the broad morphological changes in the skeleton. Alizarin red is a
190 calcium-binding dye that, combined with alcian blue (which stains polysaccharides in

191 cartilage), is routinely used to distinguish bone/cartilage. We detected alizarin red staining in
192 appendicular skeletal elements, starting in axolotls with a ST around 10-12 cm, and expanding
193 along the diaphysis to both ends as the animals grew (Fig. 2A). Alizarin red is detected in a
194 proximodistal developmental progression, from stylopod, to zeugopod and finally autopod.
195 The epiphyses of these elements remained cartilaginous in ST 20 cm animals. It is important
196 to note that alizarin red also labels mineralized cartilage, which can be seen *in vivo* in axolotls
197 by fluorescence imaging (Fig. 2B), hence it does not accurately distinguish the transition from
198 calcification to ossification. To accurately detect and quantify ossified bone volume and trace
199 the start of the ossification process, we analyzed different limbs by µCT scan. Ossification was
200 not detectable in ST 10 cm animals. The first appearance of an ossified ring around both the
201 radius and ulna was observed in animals with a ST of 12 cm (Fig. 2C). In animals bigger than
202 12 cm, ossification extended longitudinally to both ends of the bone. Interestingly, the
203 ossification did not occur homogenously, but rather with a porous appearance, resembling
204 the woven-like bone seen in mammalian bone development. In ST 25 cm animals, this porosity
205 disappeared and the tissue became uniformly ossified (Fig. 2D), forming compact bone.
206 Ossification extended to the epiphyses of the bone, as observed in the widening ends.
207 Quantification of the bone volumes (Fig. 2E) are not significantly different between bones
208 from ST 12 and 14 cm animals, or between ST 14 and 16 cm ones. However, between ST 16
209 cm and 20 cm, a 4-fold increase in bone volume was observed for the radius, and 7-fold for
210 the ulna. Moreover, radius volume was significantly higher than ulna (1.4 times increase) in
211 ST 20 cm axolotls. Even though ossification started when animals had a ST of 12 cm, there is
212 variability between siblings, especially at a ST of 14 cm (Fig. 2E). Whether this variability results
213 from sexual dimorphism or simply interindividual variation is yet to be determined.
214
215 **Zeugopodial bones are vascularized and the marrow cavity is filled with adipocytes**
216 Changes of the skeletal cellular landscape accompany the transition from a cartilage
217 anlage to bone. We assessed these changes in isolated radii from ST 6 and 12 cm axolotls,
218 which corresponded to radii before and during ossification. We performed H&E staining on
219 paraffin sections and confirmed that the radius was exclusively composed of chondrocytes in
220 ST 6 cm animals (Fig. 3A, left panel). We identified a resting zone (RZ), filled with rounded
221 chondrocytes, a proliferative zone (PZ), characterized by flattened chondrocytes, and a
222 hypertrophic zone (HZ), where chondrocyte differentiation leads to an increase in cellular

223 volume. Interestingly, these zones were not uniformly organized, as opposed to the isotropic
224 cellular distribution of mammalian growth plates. The lack of an organized cellular distribution
225 has been previously observed in another salamander model.[7] Throughout the juvenile stages,
226 a calcification ring surrounds the perichondral region of the HZ (Fig. 3A, arrowhead Fig. 3B).
227 We have observed that the first calcification ring appears early in limb development (stage
228 48) not long after hatching (stage 44), when the humerus is formed and the radius and ulna
229 have just started to form by bifurcation from the humerus distal end (according to staging
230 table[17]).

231 Radii from ST 12 cm animals (Fig. 3A, right panel) have a similar cellular distribution of
232 the cartilage region as younger animals. But in contrast to young animals, we observed the
233 formation of a primary ossification center in the diaphysis, which contained a marrow cavity
234 surrounded by cortical bone. The woven-like bone seen on the µCT scan was also observed in
235 sections as discontinuous tissue surrounding the cartilage, with defined edges between gaps
236 (arrowhead Fig. 3C). The bone extended beyond the marrow cavity, surrounding also the HZ.
237 By ST 16 cm, radii stained with H&E showed a further progression in ossification with an
238 expanding marrow cavity. However, cartilage lining subjacent to the bone is still present,
239 suggesting that the transition to bone was not completed. Embedded osteocytes in the
240 cortical bone matrix and cells lining the outer and inner sides of the bone (periosteum and
241 endosteum respectively) were observed (Fig. 3D). In both ST 12 and 16 cm, the marrow cavity
242 was filled with adipocytes, which were both identified by their morphology and by Nile red
243 staining (Fig. 3E), a lipophilic dye commonly used to identify lipid droplets.

244 A critical step for bone formation by endochondral ossification is the vascularization
245 of the tissue.[21] To assess the vascularization of the skeletal elements from ST 12 cm animals,
246 we generated a new transgenic line that expresses EGFP under the control of a *Tie2* promoter
247 and enhancer (*Tie2-Tg*),[22] labeling blood vessels in the entire animal. We collected limbs from
248 ST 6 cm animals and the radii from ST 12 cm animals and performed whole-mount
249 immunofluorescence against GFP, followed by tissue clearing and confocal imaging. We
250 observed that blood vessels surrounded the skeletal element of ST 6 cm animals, but the
251 cartilage was not vascularized (Fig. 3F, left panel). However, we observed some blood vessel
252 protrusions in close contact with the perichondrium in the HZ (arrowhead, Fig. 3G), which
253 could point to the position where the ossification of the skeletal element will start. In the radii
254 of ST 12 cm animals (Fig. 3F, right panel), the mid-diaphysis was found to be vascularized,

255 which correlates with the ossification of the cartilage anlage and formation of the marrow
256 cavity. We did not observe vascularization of the epiphyses, and thus no secondary ossification
257 center formation at this stage.
258
259 ***Sox9* marks chondrogenic cells while *Col1a2* marks all skeletal cells**
260 We identified the morphological changes of the zeugopod skeleton during growth;
261 however, the identity of the cells within the skeletal tissue, and their origin, remained unclear.
262 A key transcription factor involved in cartilage development is SOX9[13]. Thus, using a *Sox9-Tg*
263 knock in line, where a T2a self-cleaving peptide followed by mCherry protein is fused to the
264 endogenous SOX9 protein, we evaluated the distribution of mCherry$^+$ cells in ulnas from ST 6
265 and 12 cm animals (Fig. 4A). We confirmed that the expression of mCherry mirrors the real
266 expression of SOX9 by immunofluorescence (Fig. 4E). In tissue sections from ST 6 cm ulnas,
267 most cells were mCherry$^+$, while perichondral cells were mCherry$^-$ (Fig. 4A, left panel). We
268 observed a similar distribution in ulnas from ST 12 cm animals (Fig. 4A, right panel), and we
269 found no mCherry$^+$ cells in the ossified portion of the skeletal element (Fig. 4C). Moreover,
270 using a *Col1a2-Tg* line (which expresses fluorescent protein TFP under the control of the
271 *Col1a2* enhancer, labeling skeletal cells in the axolotl)[4] we evaluated the distribution of TFP$^+$
272 cells in ulnas from ST 6 and 12 cm animals (Fig. 4B). We observed TFP$^+$ cells throughout the
273 skeletal elements in both sizes, labelling both cartilage and bone cells (Fig. 4B, 4D), i.e.
274 chondrocytes, perichondral cells, osteoblasts, osteocytes and periosteal cells.
275
276 **OCN is expressed in bone cells and in some hypertrophic chondrocytes**
277 An unambiguous confirmation of ossification is the identification of mature
278 osteoblasts in the bone matrix and bone lining cells. To that end, we used immunodetection
279 of osteocalcin (anti-OCN). As expected, no labeling was observed in ulnas from ST 6 cm (Fig.
280 5A, left panel), which further demonstrated the absence of bone tissue in juvenile larvae. In
281 ST 12 cm animals, we observed a broad OCN labeling of the bone ECM (Fig. 5A, right panel).
282 We identified OCN$^+$ cells embedded in the bone matrix and in the periosteum (arrowheads,
283 Fig. 5B). Interestingly, OCN$^+$ cells were also identified in the lower HZ of the chondro-osseous
284 junction of the mid-diaphysis. These cells were mCherry$^+$, identified by our *Sox9-Tg* line (solid
285 arrowheads Fig. 5B, 5C), and SOX9$^+$, identified by sequential double immunofluorescence
286 (arrowheads Fig. 5D). Previous studies have correlated the downregulation of *Sox9* in the HZ

287 with the activation of the osteogenic program, and the persistence of SOX9 with an inhibition
288 of bone-related markers.[23,24] The expression of OCN in HCs could point towards an early
289 activation of an osteogenic program in those cells. In that regard, osteocalcin expression has
290 been reported in post-HCs.[25] Some studies have demonstrated the ability of HCs to
291 transdifferentiate into osteoblasts in mammals and zebrafish (Giovannone et al., 2019; Yang
292 et al., 2014). However, the co-expression of SOX9 and OCN needs to be further explored.
293
294 **Lineage tracing reveals a contribution of *Col1a2* cells to bone and marrow cells**
295 Our above observations led us to hypothesize that some HCs could transdifferentiate
296 into bone cells in the axolotl. To start exploring this idea, we evaluated the contribution of
297 *Col1a2* chondrocytes to bone formation.
298 Using the double transgenic *Col1a2xLPCherry-Tg*, we traced the fate of *Col1a2*
299 descendants by inducing the permanent labeling of chondrocytes by tamoxifen-induced
300 conversion of the Cre/Lox reporter cassette in ST 5 cm animals. In these animals the
301 appendicular skeleton is still exclusively cartilaginous. We allowed the animals to grow until
302 ST 14 cm and we collected the ulnas for sectioning and imaging. We observed a great
303 proportion of the cells to be mCherry$^+$. They were distributed throughout the cartilage, bone
304 matrix, periosteum, endosteum and in the marrow cavity (Fig. 6A, 6B). Moreover, we assessed
305 whether some of the mCherry$^+$ cells were OCN$^+$. We found mCherry$^+$/OCN$^+$ cells in the
306 endosteum and periosteum (arrowheads, Fig. 6C, 6C', 6C''), showing that *Col1a2* descendants
307 gave rise, at least partially, to committed osteoblasts in the axolotl zeugopod. However,
308 whether a specific subpopulation of *Col1a2* cells gives rise to all derived cells or if HCs
309 contribute directly to OCN$^+$ cells, cannot be answered with this transgenic approach.
310
311 **Bone ossification and marrow cavity expand with age**
312 Axolotls have a life span extending to more than 20-years under controlled laboratory
313 conditions.[8] However, little is known about bone morphological features in aged animals,
314 although it is commonly assumed that axolotls retain cartilaginous epiphyses and thus there
315 is perennial longitudinal growth of the bones. We collected bones and limbs from multiple 1-
316 , 5-, and 7-year-old axolotls, as well as from two animals that were 20 and 21-years of age. In
317 histological sections from radii (Fig. 7A), we observed an age-related expansion of the marrow
318 cavity towards the epiphyses. Cortical bone was also expanded longitudinally and radially,

surrounding most of the skeletal element length, even though some parts of the inner surface of the epiphyses remained cartilaginous in most cases. However, Fig. 7A shows a representative section of the 20-year-old radius, with a partial ossification of the epiphysis (arrowhead), which suggests a continuous ossification of the radius with age. Importantly, we did not identify a secondary ossification center in any of the radii analyzed. Still, we observed the appearance of marrow processes inside the hypertrophic cartilage. These longitudinal projections of the marrow cavity have been described for other salamander models.[26,27] In addition, in whole limbs stained with alcian blue/alizarin red, we observed in a 5-year-old animal a calcification in the carpal bone intermedium (Fig. 7B), as well as in 6/8 tarsal bones in our 20-year-old animal (Fig. 7C), and in 4/9 in our 21-year-old specimen. Both aged animals show ossification of the basal commune, central, intermedium and fibular tarsals. This suggests that the short bones in the autopod undergo a late ossification in comparison to the long bones in the zeugopod, but also highlights the continuity of this process in adulthood and aging.

In elements from the stylopod and autopod (digits from 2-year-old animals and humeri from 5-year-old animals) (Fig. 7D, 7E respectively), we observed the same features described for long bones in the zeugopod, i.e., an ossified ring of cortical bone around a marrow cavity filled with adipocyte tissue which expanded from the diaphysis towards the epiphyses.

This continuous ossification could be the origin of aberrant phenotypes. In 3 out of 6 7-year-old animals and in the 20-year-old animal, we observed that the zeugopodial bones were fused either in their proximal or distal epiphysis. In one case, the fusion occurred with a heterotopic ossification and cartilage formation around the distal end of the radius.

Our results show a continuous ossification of the skeletal elements even in aged animals. Whether the appendicular skeleton would become completely ossified if an animal lived long enough remains unknown.

Axolotl metamorphosis accelerates bone ossification

Metamorphosis is a critical transformation in the life cycle of many amphibians. This process allows them to access a vaster territory in their search for food and mating partners. In some anurans and urodeles, ossification of the limb skeleton is associated with the metamorphic transformation.[5,7] Although axolotls are neotenic and rarely undergo spontaneous metamorphosis, the administration of exogenous thyroxine can induce it. We

evaluated whether the ossification in axolotl is still responsive to the hormonal changes of metamorphosis. If this is the case, metamorphosis should accelerate the ossification process in axolotls. We injected thyroxine in ST 14 cm axolotls, where ossification is already covering the mid-diaphysis. Radii were collected at 35 days post-injection and embedded in paraffin for sectioning and staining. Metamorphic axolotls were slightly smaller than their paedomorph siblings, although this difference was not significant (paedomorph ST: 15.4 ± 0.4 cm, SV: 8.6 ± 0.3, n = 5, metamorphic ST: 14.7 ± 0.3, SV: 8.4 ± 0.5, n = 6). By H&E staining, we did not observe differences in the gross morphology (Fig. 8A) compared to an un-injected animal. These observations are in agreement with a previous study, in which no significant difference was observed in zeugopodial bones when surface and length were compared between a pre- and post-metamorphic axolotl.[28] However, when compared using µCT scan, we observed an increase in bone volume in metamorphic animals. Both zeugopodial bones had a bigger ossified area, and the ossification pattern was more uniform than the paedomorph bones analyzed (Fig. 8B). Bone volume quantification showed a significant increase of 4 times in radii volume and over 3 times increase for ulnas (Fig. 8C). These results demonstrate that ossification is accelerated in axolotl limbs when metamorphosis is induced, and suggest that the cells respond to intrinsic programs as well as hormonal changes.

Discussion

Appendicular skeletogenesis is considered highly conserved among tetrapods, mostly based on studies in mammals and chicks,[29] although the appendicular skeleton has undergone species-specific adaptations due to environmental influences. Many species display variations in important cellular and temporal parameters of limb development. Mammals are born with ossified bone, while most amphibians develop their limbs post-embryonically. The transition of a cartilaginous appendicular skeleton to a bony skeleton is associated with the hormonal changes during metamorphosis.[30,31] Metamorphosis in amphibians is a significant event that precedes sexual maturity, often giving the animals biological advantages, such as in their ability to acquire food or travel to new locations. In neotenic salamanders, like the axolotl, the appendicular cartilage is not only a transitional tissue; larvae live with a calcified cartilage throughout their juvenile period. Here we show that their limb skeleton continuously ossifies (in the absence of metamorphosis) until the external layer of both, epiphysis and diaphysis is completely covered by compact bone. This result contrast the previously proposed idea that the epiphyses remain cartilaginous throughout life,[26,28] and that this feature would likely contribute to longitudinal bone growth.[32]

The biological clock triggering skeletal changes remained unexplored, since axolotls rarely change to a terrestrial environment. In this work, we provide a characterization of the maturation of the appendicular skeleton during the life span of the axolotl, considering ossification timing and age-related effects, complementing previous studies in larval stages[33] and young adults.[32] In our axolotl colony, animals are grown in fully standardized conditions that allow us to use the total body length to associate it to appendicular changes and biological landmarks such as sexual maturity. During their growth, snout to vent length scales with the snout to tail length, showing a tightly controlled process. Fitting a two-line mathematical model to our normograms of ST and SV lengths evidence an explosive growth of axolotls in approximately the first 20 months of their life, after which growth velocity dramatically diminishes (Fig. 1B, 1C), however never reaching zero. To mechanistically interpret this transition age, we fitted the same normograms to a linear growth model. Our results suggest that the transition age observed in the growth velocities could be an emergent phenomenon caused by a transition in the growth rates taking place at about 10 months of age (Fig. 1D, 1G).

415 Remarkably, around this time, animals become sexually mature and ossification of their
416 appendicular bones starts, but for most of the juvenile phase axolotls present a mineralized
417 ring around the cartilaginous mid-diaphysis. Mineralization of the zeugopodial appendicular
418 skeletal elements was observed as early as developmental stage 48. In contrast, ossification
419 starts around the sexual maturity period, when we can observe the formation of a denser
420 calcified surface and embedded cells with morphological and genetic characteristics of
421 osteoblasts. Moreover, we show that *Col1a2* descendants participate in the ossification
422 process by giving rise to osteogenic cells and marrow cells (likely adipocytes). We report a
423 continuous ossification of zeugopodial bones and marrow cavity expansion with age.
424 However, this ossification is not complete, as we observed a cartilage-bone composite in most
425 of diaphyses analyzed. Short bones, such as tarsals and carpals, undergo a very late
426 ossification when compared to appendicular long bones. Finally, we see an accelerated
427 zeugopodial ossification in metamorphic animals, indicating a responsiveness to exogenous
428 thyroxine.
429
430 **Mineralization *versus* ossification**
431 For most of the initial larval stages, the skeleton is cartilaginous with mineral
432 deposition. We have observed calcification of the humeral diaphysis as early as Stage 48, when
433 the radius and ulna had just started to form by bifurcation from the humerus distal end. Nye
434 *et al*. reported mineralization by alizarin red staining at stage 50, when condensations of the
435 metacarpals are already present.[34] This discrepancy may be accounted for by the detection
436 protocol. While Nye *et al*. used processed samples, we used real-time vital detection. The
437 calcification of appendicular cartilage remains throughout the juvenile phase of the axolotl
438 until the anlage starts to ossify.
439 In contrast to mineralization, ossification is a tightly regulated process mediated by
440 osteoblast differentiation. In axolotl limbs, we can identify it around the time animals begin
441 to show secondary sexual characteristics. Generally, amphibian metamorphosis precedes
442 sexual maturation, while in neotenic amphibians both sexual maturation and bone ossification
443 occur in the absence of metamorphosis. In salamanders, as in other species, metamorphosis
444 provides adaptive features to change habitat and ensure greater chances of survival. The
445 axolotl and its geographically and phylogenetically related counterpart, *Ambystoma*
446 *velasci,*[35,36] are examples of facultative metamorphs, which means that individuals transform

447 into terrestrial organisms when the environmental conditions of its habitat change. In
448 facultative metamorphs, ossification happens independently of metamorphosis, although
449 here we questioned if metamorphosis would have an effect on ossification. We show that the
450 genetic program to trigger ossification is indeed independent of metamorphosis, but it is still
451 sensitive to exogenous thyroxine to accelerate the ossification process. In *Xenopus laevis*
452 tadpoles lacking thyroid glands, metamorphosis is halted but growth continues and
453 ossification progresses in the hind limb independently of thyroxine.[37] Together with our data,
454 this suggests that appendicular ossification programs could also be triggered in the absence
455 of L-thyroxine, and that they probably depend on a critical body mass.

456 In contrast to the fully ossified diaphysis of post-metamorphic limbs in newts
457 (*Pleurodeles waltl*),[7] the diaphysis of axolotls retains a cartilage anlage subjacent to the
458 cortical bone even in old animals, and also in post-metamorphic zeugopodial and autopodial
459 elements. We think this observation had eluded previous reports because most of them focus
460 on the humerus or humeral-radial joint. We observed in humeri of a 5-, 7- and 20-year-old
461 animals only a modest cartilage layer in the diaphysis. Although in *Xenopus* the extent of
462 ossification correlates with decreased regenerative potential, axolotls can still regenerate
463 their ossified limbs in paedomorph adults and even in induced metamorph animals.[38]
464 However, both the potential for regeneration and its fidelity are reduced.[11] Importantly, our
465 results show that ossification in the appendicular skeleton is continuous. Rux *et al.* observed
466 some degree of ossification of the metaphysis in the femur of a 10-year-old axolotl,[39] which
467 suggested that ossification of the appendicular bones continues throughout life, and here, we
468 have shown that this ossification indeed reaches the epiphyses with time.

469

470 **Contribution of *Col1a2* cells during ossification**

471 One crucial difference between axolotl and mammalian bone formation is the
472 differential activation of the *Col1a2* enhancer. In mammals only osteoblasts activate the
473 *Col1a2* enhancer,[40] while in axolotls, chondrocytes show *Col1a2* enhancer activity and COL1A2
474 and COL2A1 expression.[4,41] We have observed *Col1a2* enhancer activity as the first
475 mesenchymal condensates form in the limb bud (stage 47), and it remains active in cells inside
476 the cartilage of long bones and in HCs at the chondro-osseous junction even in 7-year-old
477 animals (personal observation).

478 One cell type largely ignored in regeneration is the adipocyte. We suggested a
479 contribution of *Col1a2* descendants to adipocytes in the marrow cavity. Although our *Col1a2-*
480 *Tg* line also labels the periosteum, its contribution to homeostasis is typically restricted to
481 skeletal cells. Therefore, we speculate that the likely contribution of *Col1a2* descendants to
482 marrow cells, such as adipocytes, is from chondrocytes. This result agrees with work done in
483 zebrafish, in which lineage tracing of chondrocytes has shown the contribution of these cells
484 to the marrow adipocytes,[14] similar to what we show in this study. Lopez *et al.* have shown
485 that the axolotl bone marrow is nonhematopoietic in young adults (1-year-old),[42] and our
486 study detects an adipocyte-filled marrow cavity in the long bones of the zeugopod in young
487 and aged animals (Fig. 3A, 3D, 3E, 7A).
488
489 **SOX9$^+$/OCN$^+$ cells**
490 During endochondral ossification, the fate of HCs is considered to be death and
491 subsequent substitution for bone cells. Unexpectedly, we found that HCs at the chondro-
492 osseous junction are SOX9$^+$/OCN$^+$. OCN is a non-collagenous protein in the bone matrix
493 expressed and secreted by committed osteoblasts. Although murine HCs can become
494 osteoblasts and osteocytes during endochondral bone formation,[14–16] it is surprising to find
495 cells expressing both SOX9 and OCN. SOX9 is known to block osteoblast differentiation and to
496 maintain columnar chondrocyte proliferation by delaying pre-hypertrophy, but also to direct
497 hypertrophic maturation.[23,24,43] The roles of SOX9 are various, and its expression in committed
498 osteoblasts has not been shown before, which suggests the presence of chondro-osteogenic
499 hybrid cells during the normal transition to the ossified skeleton in axolotl. Chondro-
500 osteogenic hybrids are generally found in reparative instances, such as in jaw regeneration in
501 zebrafish[44] and following injury in the murine rib,[45] and may hold an unexplored potential for
502 bone regeneration. In future studies, with transgenic lines labeling specifically HCs, we will be
503 able to conclusively show their contribution to different cell types in the axolotl skeleton.
504
505 **Perspectives**
506 The origin of adipocytes during ossification and their main role inside the marrow
507 cavity needs to be further explored in axolotls. The known role of bone marrow adipocytes is
508 to promote hematopoietic stem cell renewal. However, the marrow cavity of axolotls remains
509 devoid of a hematopoietic niche.[42] We assume that the adipose tissue in the marrow is white

510 fat based on morphology and the fact that brown adipose tissue has not been reported in
511 amphibians.[46] As such, it is possible that these cells have, instead, an important role in
512 osteogenesis and energy metabolism in the axolotl. Another cell type of interest is the
513 periskeletal cell. McCusker *et al*. has shown that the periskeletal tissue of older ST 25 cm
514 animals is multilayered and more complex than that of ST 6.5 cm larvae.[3] Importantly,
515 periskeletal tissue is mainly responsible for the regeneration of the skeleton.[2,3] The high
516 potential of these cells has not been tested in non-regenerative conditions, and their origin
517 and contribution to the formation of appendicular bone has not been investigated.
518
519 **Concluding remarks**
520 Taken together, our data provide evidence that bone remodeling is a
521 continuous process in axolotls, starting from a mineralized cartilaginous skeleton during the
522 larval stage to a slowly transitioning bone that continues to ossify as animals age. This
523 continuous process is accompanied by a continuous animal growth. The bone ossification
524 occurs in the absence of thyroxine or a biomechanical challenge, suggesting instead the
525 existence of a physiological timer triggered either by sexual maturation or body mass.
526 However, this ossification can be accelerated in response to exogenous thyroxine, creating in
527 a short time a bone mass that would normally take longer to form. Our findings add to a
528 growing body of literature indicating that vertebrate skeletal tissues are structurally diverse,
529 and break many of the established mammalian-centric rules of development and maturation.
530 We consider that understanding the development of the appendicular bones is essential to
531 comprehend how limb regeneration is orchestrated in stages where different cell types and
532 different maturation stages are found at the amputation plane.
533
534
535
536
537
538
539
540
541

542
543
544
545
546
547 **Methods**
548
549 **Animal husbandry, transgenesis, metamorphosis and sample collection**
550 Husbandry and experimental procedures were performed according to the Animal
551 Ethics Committee of the State of Saxony, Germany. Animals used were selected by their size,
552 which is indicated in each experiment individually (snout to tail = ST; snout to vent = SV). Sex
553 determination in juvenile larvae was performed by PCR based on. [47]
554 Axolotls (*Ambystoma mexicanum*) husbandry was performed in the CRTD axolotl
555 facility, adapted from Khattak *et al.*[18] and according to the European Directive 2010/63/EU,
556 Annex III, Table 9.1. Axolotls are kept at 18-19°C in a 12-h light/12-h dark cycle and a room
557 temperature of 20-22°C. Animals up to 2.5 cm SV are housed in individual tanks with a water
558 surface (WS) of 90 cm^2 and minimum water height (MWH) of 2.5 cm. Axolotls up to 5 cm SV
559 live in tanks with a WS of 180 cm^2 and MWH of 4.5 cm. Axolotls up to 9 cm SV live in tanks
560 with a WS of 448 cm^2 and MWH of 8 cm. Axolotl up to 11.5 cm SV live in tanks with a WS of
561 665 cm^2 and MWH of 10 cm. Axolotls of 10-15 cm SV are housed in tanks with a WS of 820-
562 1100 cm^2 with a MWH of 20 cm. Animals up to 7 cm ST are fed daily with live saltwater
563 artemia, starting at 8 cm ST they are fed with small (3mm) axolotl pellets (Aquaterratec,
564 Norgard Ambrock). Adults of 15 cm ST are fed large pellets (4-4.5 mm) twice a week.
565 White axolotls (*d/d*) were used for most of the experiments. Transgenic lines used
566 included the previously published TgSceI*(Mmus.Col1a2:TFPnls-T2a-ERT2-Cre-ERT2)*^{emt}
567 (referred to as *Col1a2-Tg*) and TgSceI*(Mmus.Col1a2:TFPnls-T2a-ERT2-Cre-*
568 *ERT2;Mmus.CAGGS:lp-GFP-3pA-lp-Cherry)*^{emt} (referred to as *Col1a2xLPCherry-Tg*).[4] We
569 generated the transgenic lines C-Ti$^{t/+}$*(Sox9:Sox9-T2a-mCherry)*^{emt} (referred as *Sox9-Tg*) and
570 TgTol2*(Mmus.Tie2:EGFP)*^{tsg} (referred to as *Tie2-Tg*).
571 For generation of the *Tie2-Tg* transgenic line, we used the plasmid pSPTg.T2FXK (#54),
572 a gift from Thomas Sato (Addgene plasmid # 35963). The *Egfp* coding region was cloned 3´
573 from the promoter together with *Tol2* sequences. Fertilized embryos from *d/d* axolotls were

574 injected with the *Tie2:EGFP* vector and *Tol2* mRNA as previously described.[18] The *Sox9-Tg*
575 reporter line is a targeted Knock-in line created by CRISPR/Cas9 technology according to the
576 published protocol.[48] Briefly, a portion of the Sox9 gene including a part of the second (last)
577 intron and the remaining downstream part of the CDS was PCRed from the axolotl genomic
578 DNA and inserted into the vector pGEM-T along with a DNA fragment encoding T2a-Cherry-
579 3xnls. The resulting vector was injected into fertilized eggs along with the CAS9 protein and
580 the gRNA targeting the sequence GGACTGCTGGCGAATGCACC, which is found in the intron
581 sequence within the vector and in the genome. As a result, mCherry fused to the C-terminus
582 of SOX9 and, separated by a T2a self-cleaving peptide, is expressed from the endogenous
583 SOX9 genomic locus.

584 Metamorphosis was induced in *d/d* animals as previously described.[18] Briefly, ST 14 cm
585 axolotls were anesthetized prior to intraperitoneal injections with 1.5 µL of L-thyroxine
586 (Sigma, T2376) per gram of bodyweight (stock 1 µg/µL in DMSO). Animals were cleaned
587 regularly and water level was reduced as gills were lost. Only 1 out of 15 animals died during
588 metamorphosis. Tissue was collected at 35 days post injection.

589 Recombination of *Col1a2xLPCherry-Tg* was induced by keeping animals in separated
590 tanks with water containing (Z)-4-hydroxytamoxifen (4-OHT, Sigma T5648) 2 µM overnight.
591 Animals were then washed and screened two weeks later to ensure conversion.

592 For tissue collection, animals were anesthetized with 0.01% benzocaine solution. After
593 collection, animals were euthanized by exposing them to a lethal dosage of anesthesia (0.1%
594 benzocaine) for at least 20 min.

595

596 **Alcian blue/alizarin red staining**

597 Limbs collected were fixed with formaldehyde 10% at 4°C for 1 week and then washed
598 three times with PBS 1x and dehydrated with serial EtOH washes (25, 50 and 70%). Limbs were
599 either stored at -20°C in EtOH 70% or processed immediately at RT. Epidermis from animals >
600 ST 12 cm was removed. Limbs were stained with alcian blue solution (Sigma A3157; alcian blue
601 0.0001% in EtOH 60% / glacial acetic acid 40%) for 3 days. Then, samples were rehydrated
602 with EtOH dilution series in H_2O (80, 70, 50, 25%), before treatment with trypsin 1% in borax
603 30% for 30 min. Limbs were rinsed with KOH 1% and stained with alizarin red solution (Sigma
604 A5533; alizarin red 0.0001% in KOH 1%) for 3 days. Next, limbs were washed with KOH 1% and
605 cleared in KOH 1% / glycerol 20% overnight. Finally, limbs were dehydrated with EtOH dilution

606 series (25, 50, 70, 90 and 3x 100%) and later transferred into serial washes of glycerol/EtOH
607 (1:3, 1:1 and 3:1). Limbs were stored in 100% glycerol at 4°C.
608
609
610
611 **µCT scan**
612 Limbs collected were fixed with formaldehyde 10% at 4°C for 1 week and then washed
613 three times with PBS 1x and dehydrated with serial EtOH washes (25, 50 and 70%) and stored
614 in EtOH 70% at -20°C until measurement. Bone volume and microarchitecture were
615 determined by micro-computed tomography (µCT, vivaCT40, ScancoMedical) of zeugopodial
616 bones using pre-defined script 6. The isotropic voxel size was 10.5 µm (70 kVp, 114 µA, 200
617 ms integration time). Diaphysis scans were done for the whole zeugopod (both elements at
618 the same time) and included 600 – 1000 slices. ScancoMedical protocols were used for all
619 analyses and 3D reconstructions. Threshold used for analyses in Fig. 2 was 220 mg HA/cm^3,
620 and for Fig. 8 was 150 mg HA/cm^3.
621
622 **Paraffin sectioning and H&E staining**
623 Skeletal elements were isolated and fixed with MEMFa 1x (MOPS 0.1M pH7.4 / EGTA
624 2mM / MgSO4x7H2O 1mM / 3.7% formaldehyde) overnight at 4°C, washed with PBS 1x and
625 decalcified with EDTA 0.5M pH7.4 at 4°C for 1 to 4 weeks. After decalcification, samples were
626 washed with PBS 1x and dehydrated with serial EtOH washes (25, 50, 70 and x3 100%).
627 Samples were then incubated 3x with Roti®Histol (Carl Roth, 6640) at RT and 4x with paraffin
628 at 65°C in glass containers. After last incubation, samples were embedded in paraffin (Roti®-
629 Plast, Carl Roth, 6642) using plastic containers and stored at RT. Longitudinal sections of 6 µM
630 thickness were obtained.
631 H&E staining on paraffin sections was performed following the producer
632 recommendations (Sigma, Procedure No. HHS).
633
634 **Cryosectioning and immunofluorescence**
635 Skeletal elements were isolated and fixed with MEMFa 1x overnight at 4°C, washed
636 with PBS 1x and decalcified with EDTA at 4°C for 48 hours. Next, the skeletal elements were
637 washed with PBS 1x and incubated overnight with sucrose 30% at 4°C. Samples were

638 embedded in O.C.T. compound (Tissue-Tek, 4583) using plastic molds and frozen with dry ice
639 for 1 hour prior to storage at -20°C. Longitudinal sections of 12 µm thickness were cut and
640 mounted on superfrost slides. Slides were kept at -20°C until processed.
641 For immunofluorescence, slides were dried at RT for at least 1 hour. Sections were
642 washed 3x with PBS 1x + 0.3% Tx-100 prior to blocking with PBS 1x + 0.3% Tx-100 + 10% normal
643 horse serum for 1 hour. Primary antibody incubation was done in blocking solution overnight
644 at 4°C. Sections were then washed 3x with PBS 1x + 0.3% Tx-100 and incubated with secondary
645 antibody 1:200 and nuclear staining 1:1000 for 2 hours. Finally, sections were washed 3x with
646 PBS 1x + 0.3% Tx-100 and mounted using Mowiol mounting medium (Carl Roth, 0713).
647 Sequential IF for SOX9/OCN was performed since the host for both antibodies is rabbit.
648 Protocol was as follows: First IF was done using the anti-SOX9 antibody as previously
649 described. Secondary antibody incubation was done using the donkey anti-rabbit, Alexa Fluor
650 488. After incubation, slides were washed three times with PBS + 0.3% Tx-100 and blocked
651 with PBS + 0.3% Tx-100 + 10% goat serum for 2 hours. Slides were incubated with anti-OCN
652 antibody in blocking solution for 1 hour at RT and then overnight at 4°C. Slides were then
653 washed 3x with PBS + 0.3% Tx-100 and incubated with goat anti-rabbit, Alexa Fluor 647
654 antibody in blocking solution for 2 hours. Slides were incubated with Hoechst 1:1000 in PBS +
655 0.3% Tx-100 for 10 min and then washed with PBS three times for 15 min. Slides were
656 mounted using Mowiol mounting medium. The antibodies and nuclear stainings used in this
657 work are listed in table 1.
658
659 **Whole mount immunofluorescence and tissue clearing**
660 Limbs or isolated skeletal elements were fixed with MEMFa 1x overnight at 4°C,
661 washed with PBS 1x and decalcified with EDTA at 4°C for 48 hours. Whole mount
662 immunofluorescence protocol was adapted from.[49] Briefly, skeletal elements were washed
663 overnight with PBS 1x + 0.3% Tx-100 at RT and then blocked in PBS + 0.3% Tx-100 + 10% DMSO
664 + 5% goat serum for 24 hours at 37°C. Samples were incubated with primary antibody anti-
665 GFP in blocking solution for 3 days at 37°C. Next, samples were briefly rinsed with PBS + 0.3%
666 Tx-100 and then washed 4x for 2 hours at 37°C. Samples were blocked again at 37°C overnight
667 and then incubated with secondary antibody for 2 days at 37°C. After incubation, samples
668 were rinsed with PBS + 0.3% Tx-100 and then washed 2x for 2 hours at 37°C. Nuclear staining

669 was done for 1 hour in washing solution at RT and samples were then washed 4x in PBS 1x for
670 15 min at RT. Isolated skeletal elements were embedded in agarose 1% before clearing.
671 For clearing, samples were dehydrated with serial washes of EtOH (25, 50, 70, 100%)
672 for 2 hours each at 4°C. Samples were then incubated overnight in EtOH 100% at 4°C prior to
673 clearing with ethyl cinnamate (Sigma, 112372-100G) at RT for at least 2 hours. Samples were
674 imaged the same day. The antibodies and nuclear stainings used in this work are listed in table
675 1.
676
677 Table 1: Antibodies and nuclear staining.

Antibody / Nuclear Staining	Dilution	Cat. Number
Anti-GFP (chicken)	1:500	Abcam (ab13970)
Anti-OCN (rabbit)	1:250	Abcam (ab198228)
Anti-SOX9 (rabbit)	1:200	Sigma-Aldrich (AB5535)
Goat anti-Rabbit, Alexa Fluor 647	1:300	Invitrogen (A-21245)
Donkey anti-Rabbit, Alexa Fluor 488	1:200	Invitrogen (A-21206)
Goat anti-Chicken, Alexa Fluor 488	1:1000	Invitrogen (A-11039)
Hoechst 33342	1:1000	Invitrogen (H3570)
TO-PRO™-3 iodide (642/661)	1:10000	Invitrogen (T3605)
SYTOX™ Green nucleic acid stain	1:10000	Invitrogen (S7020)

678
679 **Microscopy**
680 Alcian blue/alizarin red staining imaging was performed on a Zeiss Discovery.V20
681 stereomicroscope (Plan S 1.0x). H&E staining imaging was performed on a Zeiss Axio
682 Observer.Z1 inverted microscope (Plan-apochromat 20x/0.8). Immunofluorescence imaging
683 was performed on a Zeiss Axio Observer.Z1 inverted microscope with an ApoTome1 system
684 (Plan-apochromat 10x/0.45) and on a Zeiss confocal laser scanning microscope LSM 780 (Plan-
685 apochromat 10x/0.45 or Plan-apochromat 20x/0.8). Whole mount immunofluorescence
686 imaging was performed on a Zeiss confocal laser scanning microscope LSM780 (Plan
687 apochromat 10x/0.45).
688 All images were processed using Fiji.[50] Processing involved selecting regions of interest,
689 merging or splitting channels and improving brightness levels for proper presentation in
690 figures. Maximum intensity projections were done in some confocal images and it is stated in

the respective figure's descriptions. Stitching of tiles was done directly in the acquisition software Zen (Zeiss Microscopy).

Fitting the two-line model to the experimental normograms.

In this study, we fitted the following Two-line model to the normograms of ST and SV lengths:

$$L(a) = \begin{cases} L_0 + m_1 a, & a < a_t^{TL} \\ L_0 + m_1 a_t^{TL} + m_2(a - a_t^{TL}), & a \geq a_t^{TL} \end{cases}$$

Where, $L(a)$ is the ST or SV length at age a, L_0 is the ST or SV length at age zero. The four model free-parameters are m_1 is the slope of the first line, a_t^{TL} is the transition time of this model and m_2 is the slope of the second line.

In our normograms, each value represents a single animal. By fitting the model to the experimental data and using bootstrapping, we estimated the parameter values together with their errors from the ST (table 2) and SV (table 3) lengths:

Table 2: Estimation of the Two-Line model parameters from the normogram of ST lengths.

Two-Line model parameters	**Value ± Error (Units)**
L_0	0 ± 1 (10^{-14} cm)
m_1	1.144 ± 0.003 (cm/month)
m_2	0.0325 ± 0.0006 (cm/month)
a_t^{TL}	19.87 ± 0.07 (month)

Table 3: Estimation of the Two-Line model parameters from the normogram of SV lengths.

Two-Line model parameters	**Value ± Error (Units)**
L_0	8 ± 2 (10^{-16} cm)
m_1	0.618 ± 0.002 (cm/month)
m_2	0.0202 ± 0.0004 (cm/month)
a_t^{TL}	19.00 ± 0.07 (month)

Fitting the growth model to the experimental normograms

In this study, we fitted the following linear growth model to the normograms of ST and SV lengths:

$$\frac{dL}{da} = r(a) * L$$

Where, L is the ST or SV length at age a and $r(a)$ is the growth rate (depending on the age a), defined as follows:

$$r(a) = r_\infty + \frac{r_0 - r_\infty}{1 + \left(\frac{a}{a_t^{GR}}\right)^n}$$

The model free-parameters are the r_0, r_∞, n and a_t^{GR}, the growth rate at age zero, the growth rate at infinite age, the Hill-exponent denoting sigmoidicity and the growth rate transition age, respectively.

By fitting the model to the experimental data and using bootstrapping, we estimated the parameter values together with their errors from the ST (table 4) and SV (table 5) lengths.

Table 4: Estimation of the linear growth model parameters from the normogram of ST lengths.

Growth model parameters	**Value ± Error (Units)**
r_0	0.323 ± 0.002 (1/month)
r_∞	0.00116 ± 0.00003 (1/month)
n	5.6 ± 0.07 (−)
a_t^{GR}	9.87 ± 0.05 (month)

Table 5: Estimation of the linear growth model parameters from the normogram of SV lengths.

Growth model parameters	**Value ± Error (Units)**
r_0	0.247 ± 0.001 (1/month)
r_∞	0.00142 ± 0.00002(1/month)
n	7.8 ± 0.1 (−)
a_t^{GR}	11.07 ± 0.05(month)

Jupyter Notebook (http://jupyter.org/) containing the source code for all computations performed and referred to as Riquelme-Guzmán et al., 2021 in this study can be found at https://doi.org/10.5281/zenodo.5033614. [51]

742 **Statistical analysis**

743 Statistical analysis was performed using the software Prism9 (GraphPad Software, LLC)
744 for macOS. To assess the differences in ST or SV between sexes (Fig. 1H), a paired t test was
745 performed between samples. To assess the differences in volume between radii and ulnas of
746 different ST animals (Fig. 2E) and between radii and ulnas of paedomorph and metamorphic
747 animals (Fig. 8C), a Two-way ANOVA test was performed, using a post hoc Tukey's multiple
748 comparisons test for assessing statistical significance between each sample pair. P-values <
749 0.05 were considered statistically significant.

750
751
752
753
754
755
756
757
758
759
760
761
762
763
764
765
766
767
768
769
770
771
772
773

Acknowledgements

We would like to thank Elly M. Tanaka for providing the *Sox9-Tg* line and Joshua D. Currie for guidance during the creation of the *Tie2-Tg* line. We thank Prof. Lorenz Hofbauer, Osvaldo Contreras, Rita Aires and Sean Keeley for proof-reading this paper and for their valuable comments. We thank all members of the Sandoval-Guzmán Lab for continuous support during the development of this work. We also would like to thank Anja Wagner, Beate Gruhl and Judith Konantz for their valuable dedication to the axolotl care. This work was funded by a DFG Research Grant (SA 3349/3-1). CRG was supported by the DIGS-BB Fellow award. AC and OC were funded by Consejo Nacional de Investigaciones Científicas y Técnicas (CONICET) of Argentina and by the grant from Agencia Nacional de Promoción Científica y Tecnológica (ANPCyT) PICT-2017-2307. AC was supported by a doctoral scholarship program from CONICET. OC is a career researcher from CONICET. This work was supported by the Light Microscopy Facility, a Core Facility of the CMCB Technology Platform at TU Dresden.

Authors contribution

CRG and TSG conceived experiments, analysed data and wrote the manuscript. CRG conducted experiments. MR, MS, AB and SE contributed experimental data and support. AC and OC performed the mathematical modelling. DK created *Sox9-Tg* line. DK, OC and MR contributed with manuscript revision and discussions. TSG secured funding for the project.

806

807

808

809

810 **References**

811

812 1. Kragl M, Knapp D, Nacu E, et al. Cells keep a memory of their tissue origin during axolotl
813 limb regeneration. *Nature*. 2009;460(7251):60-65. doi:10.1038/nature08152

814 2. Currie JD, Kawaguchi A, Traspas R, Schuez M, Chara O, Tanaka EM. Live Imaging of Axolotl
815 Digit Regeneration Reveals Spatiotemporal Choreography of Diverse Connective Tissue
816 Progenitor Pools. *Dev Cell*. 2016;39(4):411-423. doi:10.1016/j.devcel.2016.10.013

817 3. McCusker CD, Diaz-Castillo C, Sosnik J, Phan AQ, Gardiner DM. Cartilage and bone cells do
818 not participate in skeletal regeneration in Ambystoma mexicanum limbs. *Dev Biol*.
819 2016;416(1):26-33. doi:10.1016/j.ydbio.2016.05.032

820 4. Gerber T, Murawala P, Knapp D, et al. Single-cell analysis uncovers convergence of cell
821 identities during axolotl limb regeneration. *Science*. 2018:eaaq0681.
822 doi:10.1126/science.aaq0681

823 5. Miura S, Hanaoka K, Togashi S. Skeletogenesis in Xenopus tropicalis: Characteristic bone
824 development in an anuran amphibian. *Bone*. 2008;43(5):901-909.
825 doi:10.1016/j.bone.2008.07.005

826 6. Rozenblut B, Ogielska M. Development and growth of long bones in European water frogs
827 (Amphibia: Anura: Ranidae), with remarks on age determination. *J Morphol*.
828 2005;265(3):304-317. doi:10.1002/jmor.10344

829 7. Quilhac A, Ricqlès A, Lamrous H, Zylberberg L. Globuli ossei in the long limb bones of
830 Pleurodeles waltl (Amphibia, Urodela, Salamandridae). *J Morphol*. 2014;275(11):1226-1237.
831 doi:10.1002/jmor.20296

832 8. Vieira WA, Wells KM, McCusker CD. Advancements to the Axolotl Model for Regeneration
833 and Aging. *Gerontology*. 2019:1-11. doi:10.1159/000504294

834 9. Malacinski GM. The Mexican Axolotl, Ambystoma mexicanum: Its Biology and
835 Developmental Genetics, and Its Autonomous Cell-lethal Genes. *Integr Comp Biol*.
836 1978;18(2):195-206. doi:10.1093/icb/18.2.195

837 10. Wolfe A, Nye H, Cameron J. Extent of ossification at the amputation plane is correlated
838 with the decline of blastema formation and regeneration in Xenopus laevis hindlimbs. *Dev*
839 *Dyn*. 2000;218(4):681-697. doi:10.1002/1097-0177(2000)9999:9999<::AID-
840 DVDY1018>3.0.CO;2-6

841 11. Monaghan JR, Stier AC, Michonneau F, et al. Experimentally induced metamorphosis in
842 axolotls reduces regenerative rate and fidelity. *Regen*. 2014;1(1):2-14. doi:10.1002/reg2.8

843 12. Olsen B, Reginato A, Wang W. Bone development. *Annual review of cell and*
844 *developmental biology*. 2000;16:191-220. doi:10.1146/annurev.cellbio.16.1.191

845 13. Kozhemyakina E, Lassar AB, Zelzer E. A pathway to bone: signaling molecules and
846 transcription factors involved in chondrocyte development and maturation. *Development*.
847 2015;142(5):817-831. doi:10.1242/dev.105536

848 14. Giovannone D, Paul S, Schindler S, et al. Programmed conversion of hypertrophic
849 chondrocytes into osteoblasts and marrow adipocytes within zebrafish bones. *ELife*. 2019;8.
850 doi:10.7554/eLife.42736

851 15. Yang L, Tsang K, Tang H, Chan D, Cheah KS. Hypertrophic chondrocytes can become
852 osteoblasts and osteocytes in endochondral bone formation. *PNAS*. 2014;111(33):12097-
853 12102. doi:10.1073/pnas.1302703111

854 16. Jing Y, Jing J, Ye L, et al. Chondrogenesis and osteogenesis are one continuous
855 developmental and lineage defined biological process. *Sci Rep*. 2017;7(1):10020.
856 doi:10.1038/s41598-017-10048-z

857 17. Schreckenberg GM, Jacobson AG. Normal stages of development of the axolotl,
858 Ambystoma mexicanum. *Dev Biol*. 1975;42(2):391-399. doi:10.1016/0012-1606(75)90343-7

859 18. Khattak S, Murawala P, Andreas H, et al. Optimized axolotl (Ambystoma mexicanum)
860 husbandry, breeding, metamorphosis, transgenesis and tamoxifen-mediated recombination.
861 *Nat Protoc*. 2014;9(3):529-540. doi:10.1038/nprot.2014.040

862 19. Rost F, Albors AR, Mazurov V, et al. Accelerated cell divisions drive the outgrowth of the
863 regenerating spinal cord in axolotls. *Elife*. 2016;5:e20357. doi:10.7554/elife.20357

864 20. Costa EC, Otsuki L, Albors AR, Tanaka EM, Chara O. Spatiotemporal control of cell cycle
865 acceleration during axolotl spinal cord regeneration. *Elife*. 2021;10:e55665.
866 doi:10.7554/elife.55665

867 21. Filipowska J, Tomaszewski KA, Niedźwiedzki Ł, Walocha JA, Niedźwiedzki T. The role of
868 vasculature in bone development, regeneration and proper systemic functioning.
869 *Angiogenesis*. 2017;20(3):291-302. doi:10.1007/s10456-017-9541-1

870 22. Schlaeger TM, Bartunkova S, Lawitts JA, et al. Uniform vascular-endothelial-cell-specific
871 gene expression in both embryonic and adult transgenic mice. *PNAS*. 1997;94(7):3058-3063.
872 doi:10.1073/pnas.94.7.3058

873 23. Dy P, Wang W, Bhattaram P, et al. Sox9 Directs Hypertrophic Maturation and Blocks
874 Osteoblast Differentiation of Growth Plate Chondrocytes. *Dev Cell*. 2012;22(3):597-609.
875 doi:10.1016/j.devcel.2011.12.024

24. Lui JC, Yue S, Lee A, et al. Persistent Sox9 expression in hypertrophic chondrocytes suppresses transdifferentiation into osteoblasts. *Bone*. 2019;125:169-177. doi:10.1016/j.bone.2019.05.027

25. Pullig O, Weseloh G, Ronneberger D-L, Käkönen S-M, Swoboda B. Chondrocyte Differentiation in Human Osteoarthritis: Expression of Osteocalcin in Normal and Osteoarthritic Cartilage and Bone. *Calcified Tissue Int*. 2000;67(3):230-240. doi:10.1007/s002230001108

26. Haines RW. The Evolution of Epiphyses and of Endochondral Bone. *Biol Rev Camb Philos Soc*. 1942. doi:https://doi.org/10.1111/j.1469-185X.1942.tb00440.x

27. Molnar JL. Variation in Articular Cartilage Thickness Among Extant Salamanders and Implications for Limb Function in Stem Tetrapods. *Frontiers Ecol Evol*. 2021;9:671006. doi:10.3389/fevo.2021.671006

28. Thampi P, Liu J, Zeng Z, MacLeod JN. Changes in the appendicular skeleton during metamorphosis in the axolotl salamander (Ambystoma mexicanum). *J Anat*. 2018;233(4):468-477. doi:10.1111/joa.12846

29. Shubin N, Tabin C, Carroll S. Fossils, genes and the evolution of animal limbs. *Nature*. 1997;388(6643):639-648. doi:10.1038/41710

30. Kemp NE, Hoyt JA. Sequence of ossification in the skeleton of growing and metamorphosing tadpoles of Rana pipiens. *J Morphol*. 1969;129(4):415-443. doi:10.1002/jmor.1051290404

31. Rose CS, Reiss JO. Metamorphosis and the vertebrate skull: ontogenetic patterns and developmental mechanisms. In: Hanken J, Hall BK, eds. *The Skull*. Vol 1. University of Chicago Press; 1993:289-346.

32. Cosden-Decker RS, Bickett MM, Lattermann C, MacLeod JN. Structural and functional analysis of intra-articular interzone tissue in axolotl salamanders. *Osteoarthr Cartil*. 2012;20(11):1347-1356. doi:10.1016/j.joca.2012.07.002

33. Torok MA, Gardiner DM, Shubin NH, Bryant SV. Expression of HoxD Genes in Developing and Regenerating Axolotl Limbs. *Dev Biol*. 1998;200(2):225-233. doi:10.1006/dbio.1998.8956

34. Nye HLD, Cameron JA, Chernoff EAG, Stocum DL. Extending the table of stages of normal development of the axolotl: Limb development. *Dev Dyn*. 2003;226(3):555-560. doi:10.1002/dvdy.10237

35. Shaffer HB, McKnight ML. The Polytypic Species Revisited: Genetic Differentiation and Molecular Phylogenetics of the Tiger Salamander Ambystoma tigrinum (Amphibia: Caudata) Complex. *Evolution*. 1996;50(1):417. doi:10.2307/2410811

36. Parra-Olea G, Recuero E, Zamudio KR. Polymorphic microsatellite markers for Mexican salamanders of the genus Ambystoma. *Mol Ecol Notes*. 2007;7(5):818-820. doi:10.1111/j.1471-8286.2007.01714.x

913 37. Kerney R, Wassersug R, Hall BK. Skeletal advance and arrest in giant non-
914 metamorphosing African clawed frog tadpoles (Xenopus laevis: Daudin). *J Anat*.
915 2010;216(1):132-143. doi:10.1111/j.1469-7580.2009.01176.x

916 38. Young HE, Bailey CF, Markwald RR, Dalley BK. Histological analysis of limb regeneration in
917 postmetamorphic adult Ambystoma. *Anatomical Rec*. 1985;212(2):183-194.
918 doi:10.1002/ar.1092120213

919 39. Rux D, Decker RS, Koyama E, Pacifici M. Joints in the appendicular skeleton:
920 Developmental mechanisms and evolutionary influences. *Curr Top Dev Biol*. 2018;133:119-
921 151. doi:10.1016/bs.ctdb.2018.11.002

922 40. Bou-Gharios G, Garrett LA, Rossert J, et al. A potent far-upstream enhancer in the mouse
923 pro alpha 2(I) collagen gene regulates expression of reporter genes in transgenic mice. *J Cell*
924 *Biology*. 1996;134(5):1333-1344. doi:10.1083/jcb.134.5.1333

925 41. Khattak S, Schuez M, Richter T, et al. Germline transgenic methods for tracking cells and
926 testing gene function during regeneration in the axolotl. *Stem Cell Rep*. 2013;1(1):90-103.
927 doi:10.1016/j.stemcr.2013.03.002

928 42. Lopez D, Lin L, Monaghan JR, et al. Mapping hematopoiesis in a fully regenerative
929 vertebrate: the axolotl. *Blood*. 2014;124(8):1232-1241. doi:10.1182/blood-2013-09-526970

930 43. Hattori T, Müller C, Gebhard S, et al. SOX9 is a major negative regulator of cartilage
931 vascularization, bone marrow formation and endochondral ossification. *Development*.
932 2010;137(6):901-911. doi:10.1242/dev.045203

933 44. Paul S, Schindler S, Giovannone D, Terrazzani A de M, Mariani FV, Crump JG. Ihha induces
934 hybrid cartilage-bone cells during zebrafish jawbone regeneration. *Development*.
935 2016;143(12):2066-2076. doi:10.1242/dev.131292

936 45. Kuwahara ST, Serowoky MA, Vakhshori V, et al. Sox9+ messenger cells orchestrate large-
937 scale skeletal regeneration in the mammalian rib. *Elife*. 2019;8:e40715.
938 doi:10.7554/elife.40715

939 46. Gesta S, Tseng Y-H, Kahn CR. Developmental Origin of Fat: Tracking Obesity to Its Source.
940 *Cell*. 2007;131(2):242-256. doi:10.1016/j.cell.2007.10.004

941 47. Keinath MC, Timoshevskaya N, Timoshevskiy VA, Voss SR, Smith JJ. Miniscule differences
942 between sex chromosomes in the giant genome of a salamander. *Sci Rep*. 2018;8(1):17882.
943 doi:10.1038/s41598-018-36209-2

944 48. Fei J-F, Lou WP-K, Knapp D, et al. Application and optimization of CRISPR–Cas9-mediated
945 genome engineering in axolotl (Ambystoma mexicanum). *Nat Protoc*. 2018;13(12):2908-
946 2943. doi:10.1038/s41596-018-0071-0

947 49. Masselink W, Reumann D, Murawala P, et al. Broad applicability of a streamlined Ethyl
948 Cinnamate-based clearing procedure. *Development*. 2019;146(3):dev.166884.
949 doi:10.1242/dev.166884

50. Schindelin J, Arganda-Carreras I, Frise E, et al. Fiji: an open-source platform for biological-image analysis. *Nat Methods*. 2012;9(7):676-682. doi:10.1038/nmeth.2019

51. Riquelme-Guzmán C, Schuez M, Böhm A, et al. Post-embryonic development and aging of the appendicular skeleton in Ambystoma mexicanum. *Zenodo*. 2021;(Supplementary Notebooks – v1.0). doi:https://doi.org/10.5281/zenodo.5033614

Figure legends

Figure 1. Axolotls transitions from a rapid to a slower growth phase at about 10 months of age.

(A) Snout to tail length (ST) linearly correlates snout to vent length (SV) in n = 220 axolotls of different ages (dots). Color code represents age in months. The line shows a linear regression to the experimental data.

(B - C) Normogram of ST (B) and SV (C) lengths versus axolotl age (dots, same data shown in A). A two-line model was fitted to the experimental data (the continuous lines depict the best-fitting simulation).

(D - E) A growth model was fitted to the experimental ST (D) and SV (E) lengths (dots, same data shown in A, B and C; the continuous lines depict the best-fitting simulation).

(F - G) Time course of the Growth rate predicted by the growth model fitted to the ST (F) and SV (G). Insets show magnification of the age near the transition age (vertical lines) of 9.87 ± 0.05 and 11.07 ± 0.05 months for the ST (F) and SV (G) lengths respectively.

(H) Quantification of ST and SV lengths in cm in 1-year-old siblings as a function of its sex. (n = 18, 9 males and 9 females. *** $p < 0.001$, Student's t test).

Figure 2: The zeugopodial skeleton is progressively ossified with growth.

(A) Alcian blue/alizarin red staining of limbs from different ST animals (n = 4). R: radius, U: ulna. Scale bar: 500 µm.

976 (B) *In vivo* alizarin red staining of axolotl ST 5 cm. Scale bar: 500 µm

977 (C) 3D reconstructions from µCT scan for zeugopodial bones from different ST animals (n =
978 4). All bones are scaled. Scale bar: 250 µm.

979 (D) 3D reconstruction from µCT scan for zeugopodial bones from ST 25 cm axolotl (n = 1).
980 Bones scaled to (C). Scale bar: 500 µm.

981 (E) Quantification of zeugopodial bones volume (cm^3) from different ST animals. (n = 4 per
982 size. a: radius ST 20 cm compared to radius from ST 10, 12, 14 and 16 cm. b: ulna ST 20 cm
983 versus ulna from ST 10, 12, 14 and 16 cm. c: radius ST 20 cm versus ulna ST 20 cm. a, b: $p <$
984 0.001, c: $p < 0.05$, Tukey's multiple comparisons test).

985

986 **Figure 3: Zeugopodial bones are vascularized and the marrow cavity is filled with adipocytes.**

987 (A) H&E staining from radii from axolotls ST 6 and 12 cm (n = 6). RZ: resting zone, PZ:
988 proliferative zone, HZ: hypertrophic zone, MC: marrow cavity, D: distal, P: proximal. Scale bar:
989 500 µm.

990 (B) Inset from ST 6 cm in (A). Arrowhead: calcified ring around HZ. Scale bar: 250 µm

991 (C) Inset from ST 12 cm in (A). Arrowhead: discontinuous ossification around diaphysis. Scale
992 bar: 250 µm

993 (D) H&E staining in the distal half of the radius from a ST 16 cm axolotl (n = 6). Scale bar: 500
994 µm.

995 (E) Nile red staining in marrow cavity of a ST 14 cm axolotl (n = 3). c: cartilage, b: bone, mc:
996 marrow cavity. Scale bar: 100 µm.

997 (F) Confocal image of anti-GFP whole mount IF of forelimb or radius from *Tie2-Tg* (red) ST 6 or
998 12 cm animals, respectively (n = 4). TO-PRO™3 was used for nuclear staining (white). Image
999 represent a maximum intensity projection of 3 images (10 µm interval). Arrowheads: bone
1000 vascularization. Scale bar: 250 µm.

1001 (G) Inset from *Tie2-Tg* ST 6 cm in (F) with overlapping brightfield image. Arrowhead: blood
1002 vessel in contact with calcified cartilage. Scale bar: 100 µm.

1003

1004

1005

1006 **Figure 4: *Sox9* marks chondrogenic cells while *Col1a2* marks all skeletal cells.**

1007 (A) Confocal image of *Sox9-Tg* (red), ulnas sections from ST 6 and 12 cm axolotls (n = 6).
1008 Calcified tissue stained with calcein (green). TO-PRO™3 was used for nuclear staining
1009 (white). D: distal, P: proximal. Scale bar: 250 µm.

1010 (B) Confocal image of *Col1a2-Tg* (red) ulna sections from ST 6 and 12 cm axolotls (n = 6). TO-
1011 PRO™3 was used for nuclear staining (white). Scale bar: 250 µm.

1012 (C) Inset from (A) *Sox9-Tg* ST 12 cm. Dotted line shows boundary between cartilage and
1013 bone (chondro-osseous junction), hc: hypertrophic chondrocytes. Scale bar: 250 µm.

1014 (D) Inset from (B) *Col1a2-Tg* ST 12 cm. os: osteocyte, eo: endosteal cell, hc: hypertrophic
1015 chondrocytes. Scale bar: 250 µm.

1016 (E) Confocal image of anti-SOX9 IF in ulna sections from *Sox9-Tg* in ST 16 cm axolotl (n = 3).
1017 SYTOX™ Green was used for nuclear staining. Scale bar: 250 µm.

1018

1019 **Figure 5: OCN is expressed in bone cells and in some hypertrophic chondrocytes.**

1020 (A) Apotome image of anti-OCN IF (red) from representative radii sections from ST 6 and 12
1021 cm axolotls (n = 6). SYTOX™ Green was used for nuclear staining (white). D: distal, P:
1022 proximal. Scale bar: 250 µm.

1023 (B) Inset from (A) anti-OCN IF (red). Dotted line shows boundary between cartilage and
1024 bone. Solid arrowhead: hypertrophic chondrocytes. Arrowhead: periosteal cells. Scale bar:
1025 100 µm.

1026 (C) Confocal image of anti-OCN IF from radius section from *Sox9-Tg* ST 12 cm (n = 3). SYTOX™
1027 Green was used for nuclear staining. Scale bar: 100 µm.

1028 (D) Confocal image of sequential IF for anti-SOX9 and anti-OCN in ST 16 cm axolotls (n = 4).
1029 Hoechst 33342 was used for nuclear staining. Image represent a maximum intensity
1030 projection of 4 images (2 µm interval). Arrowheads: $SOX9^+/OCN^+$ cells. Scale bar: 50 µm.

1031 **Figure 6: Lineage tracing reveals a contribution of *Col1a2*$^+$ cells to bone and marrow cells.**

1032 (A) Confocal image of *Col1a2xLPCherry-Tg* (red) ulna sections from ST 14 cm axolotls (n = 6).
1033 SYTOX™ Green was used for nuclear staining (white). Dotted line shows boundary between
1034 cartilage and bone, c: cartilage, b: bone, mc: marrow cavity. Scale bar: 250 µm.

1035 (B) Confocal image of *Col1a2xLPCherry-Tg* (red) ulna sections from ST 14 cm axolotls (n = 6).
1036 SYTOX™ Green was used for nuclear staining (white). Arrowhead: $mCherry^+$ cells. po:
1037 periosteum, eo: endosteum, mc: marrow cavity. Scale bar: 100 µm.

1038 (C-C'') Confocal image of anti-OCN IF (green) from ulna sections from *Col1a2xLPCherry-Tg*
1039 (red) ST 14 cm axolotls (n = 6). SYTOX™ Green was used for nuclear staining (white).
1040 Arroheads: $mCherry^+/OCN^+$ cells. Scale bar: 100 µm.

1041

1042 **Figure 7: Bone ossification and marrow cavity expand with age.**

1043 (A) H&E staining of radii sections from different age axolotls (n = 6 for 11-month-old, n = 3
1044 for 5-year-old, n = 5 for 7-year-old, n = 1 for 20-year-old). D: distal, P: proximal, ep:
1045 epiphysis, mc: marrow cavity, b: bone. Scale bar: 500 µm.

1046 (B) Alcian blue/alizarin red staining of forelimb from a 5-year-old axolotl (n = 3). bc, basale
1047 commune; c, centrale; i, intermedium; r, radiale; u, ulnare. Scale bar: 2 mm.

1048 (C) Alcian blue/alizarin red staining of foot from a 20-year-old axolotl (n = 1). bc, basale
1049 commune; c, centrale; i, intermedium; t, tibiale; f, fibulare; y, element y. Scale bar: 2 mm.

1050 (D) H&E staining of proximal phalanx from 2-year-old axolotl (n = 4). Scale bar: 1 mm.

1051 (E) H&E staining of humerus from 5-year-old axolotl (n = 2). Scale bar: 1 mm.

1052

1053 **Figure 8: Axolotl metamorphosis accelerates bone ossification**

1054 (A) H&E staining from radii sections from paedomorph and metamorphic axolotls (35 dpi) (n
1055 = 4). D: distal, P: proximal. Scale bar: 500 µm.

1056 (B) 3D reconstructions from µCT scan for zeugopodial bones from paedomorph and
1057 metamorphic axolotl (n = 5 for paedomorph zeugopods, n = 6 for metamorphic zeugopods).
1058 All bones are scaled. R: radius, U: ulna. Scale bar: 500 µm.

1059 (C) Quantification of zeugopodial bones volume (cm^3) from paedomorph and metamorphic
1060 axolotl. (n = 5 for paedomorph zeugopods, n = 6 for metamorphic zeugopods. ** $p < 0.01$, *
1061 $p < 0.05$, Tukey's multiple comparisons test).

1062

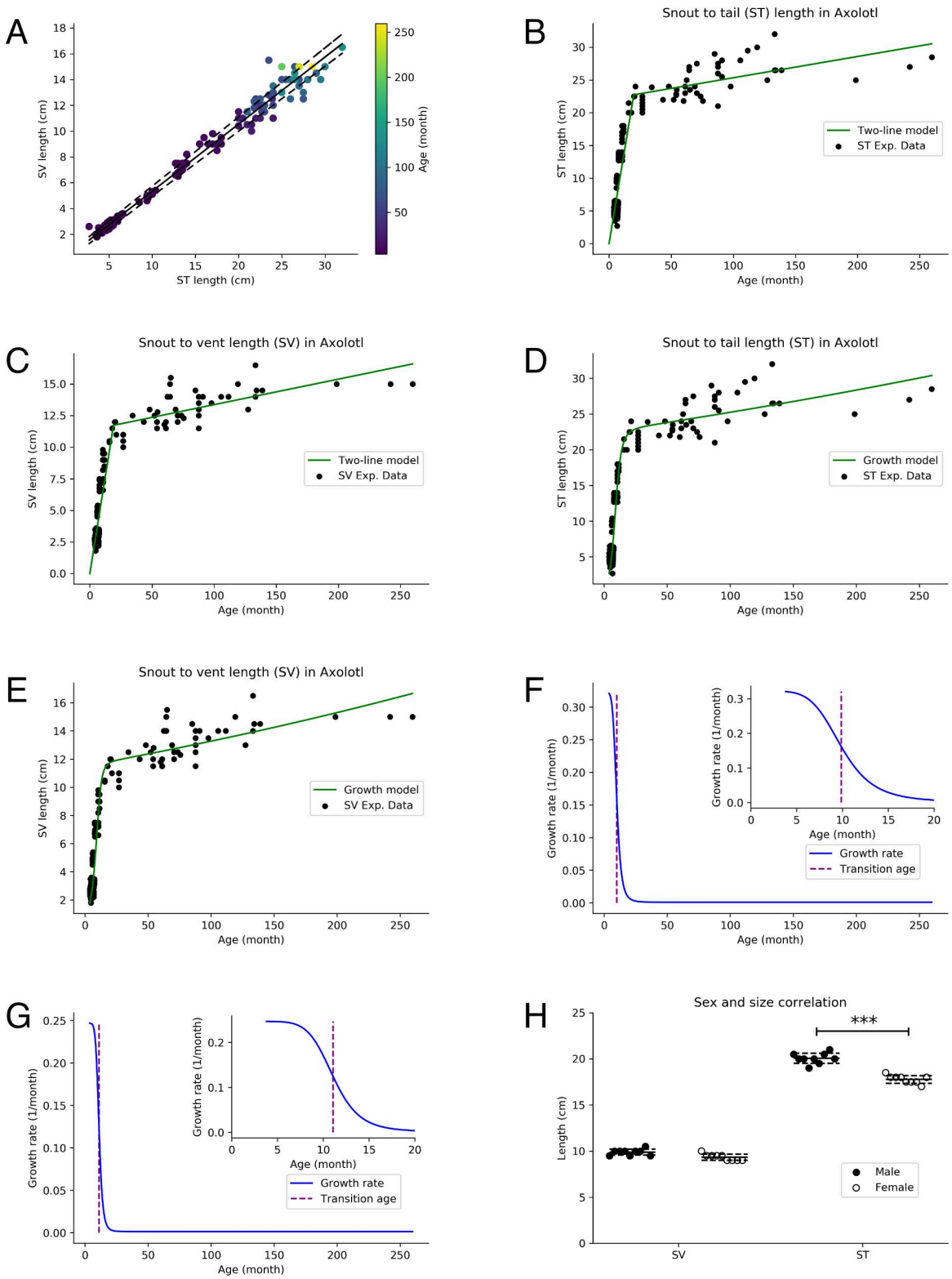
A
SV length (cm)
ST length (cm)
Age (month)
B
Snout to tail (ST) length in Axolotl
ST length (cm)
Age (month)
Two-line model
ST Exp. Data
C
Snout to vent length (SV) in Axolotl
SV length (cm)
Age (month)
Two-line model
SV Exp. Data
D
Snout to tail length (ST) in Axolotl
ST length (cm)
Age (month)
Growth model
ST Exp. Data
E
Snout to vent length (SV) in Axolotl
SV length (cm)
Age (month)
Growth model
SV Exp. Data
F
Growth rate (1/month)
Age (month)
Growth rate
Transition age
G
Growth rate (1/month)
Age (month)
Growth rate
Transition age
H
Sex and size correlation
***
Length (cm)
SV
ST
Male
Female

1063

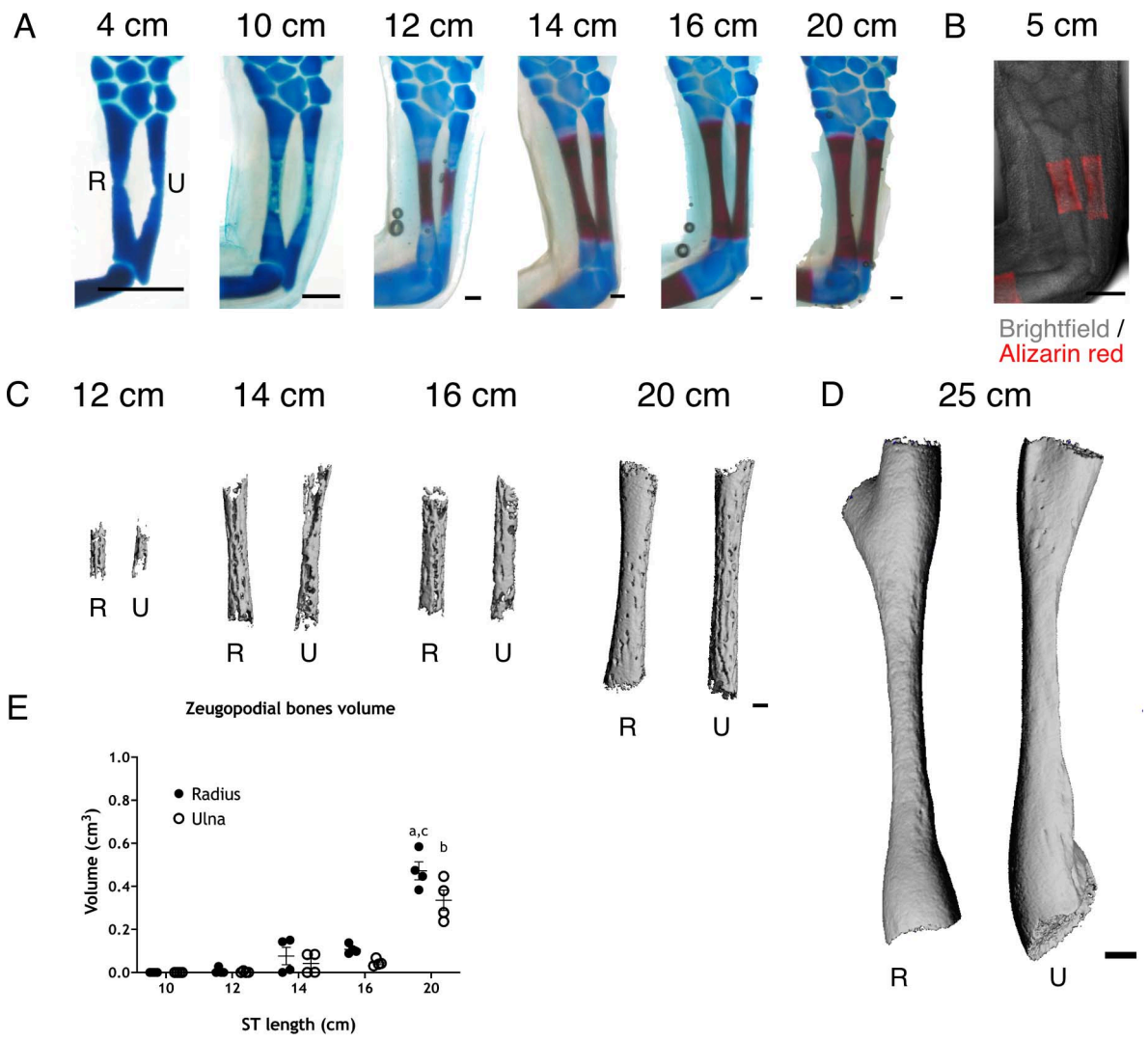
A
4 cm
10 cm
12 cm
14 cm
16 cm
20 cm
B
5 cm
R
U
Brightfield /
Alizarin red
C
12 cm
14 cm
16 cm
20 cm
D
25 cm
R
U
E
Zeugopodial bones volume
Radius
Ulna
Volume (cm³)
ST length (cm)
a,c
b

1064

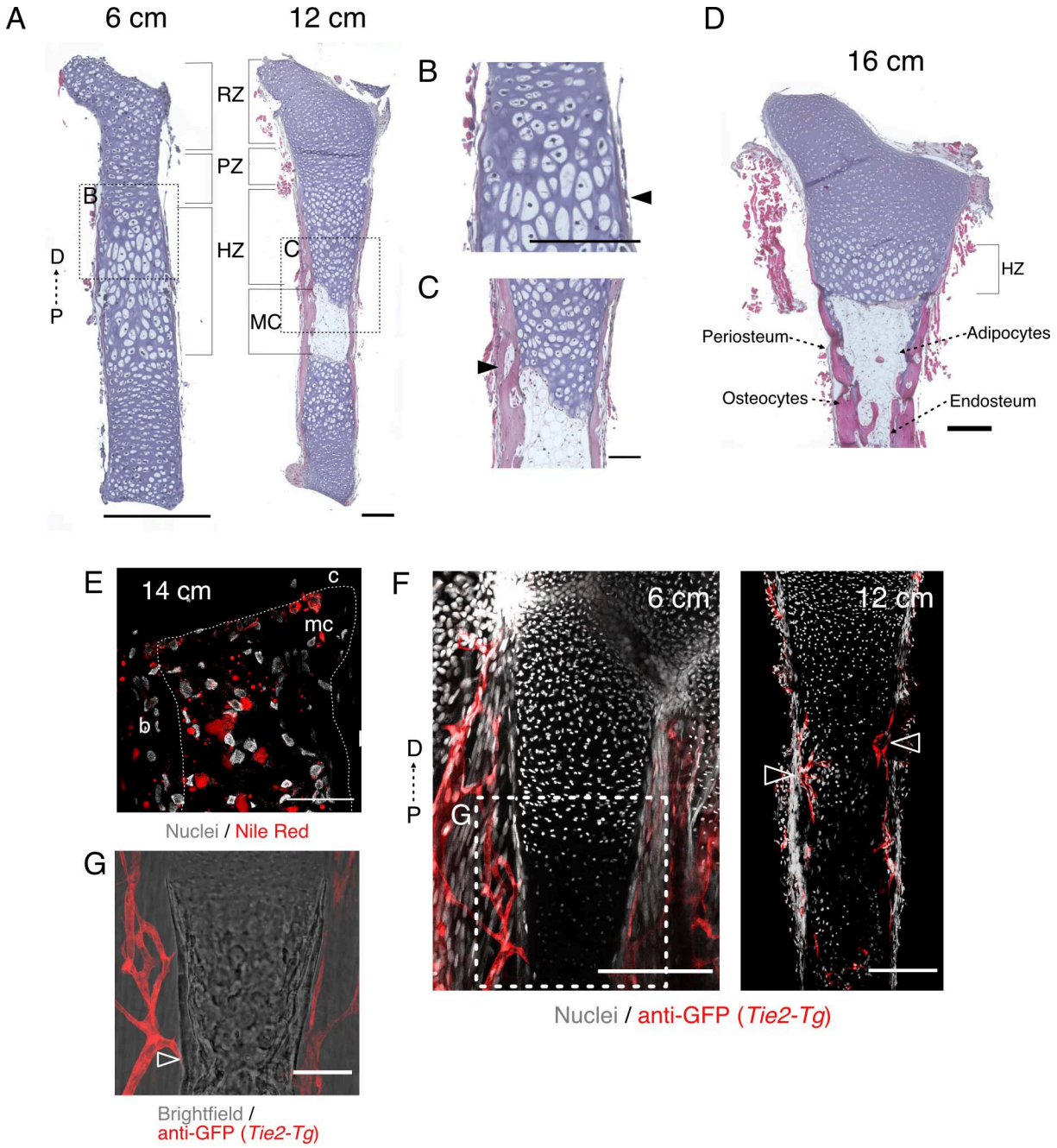
A
6 cm
12 cm
RZ
PZ
HZ
MC
B
C
D
P
B
C
D
16 cm
HZ
Periosteum
Adipocytes
Osteocytes
Endosteum
E
14 cm
c
mc
b
Nuclei / Nile Red
F
6 cm
12 cm
D
P
G
Nuclei / anti-GFP (Tie2-Tg)
G
Brightfield /
anti-GFP (Tie2-Tg)

1065

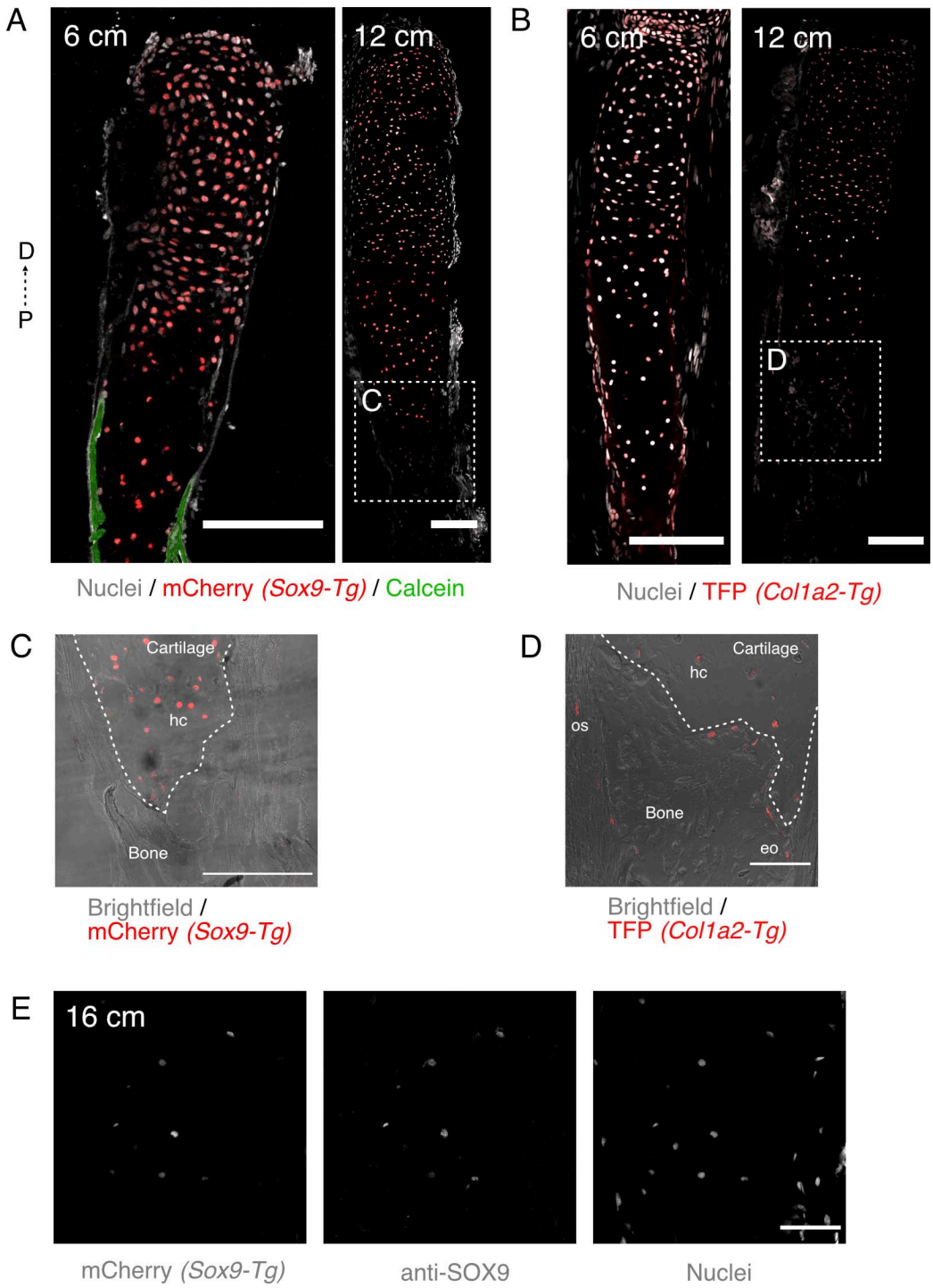
A
6 cm
12 cm
D
P
C
Nuclei / mCherry (Sox9-Tg) / Calcein
B
6 cm
12 cm
D
Nuclei / TFP (Col1a2-Tg)
C
Cartilage
hc
Bone
Brightfield /
mCherry (Sox9-Tg)
D
Cartilage
hc
os
Bone
eo
Brightfield /
TFP (Col1a2-Tg)
E
16 cm
mCherry (Sox9-Tg)
anti-SOX9
Nuclei

1066

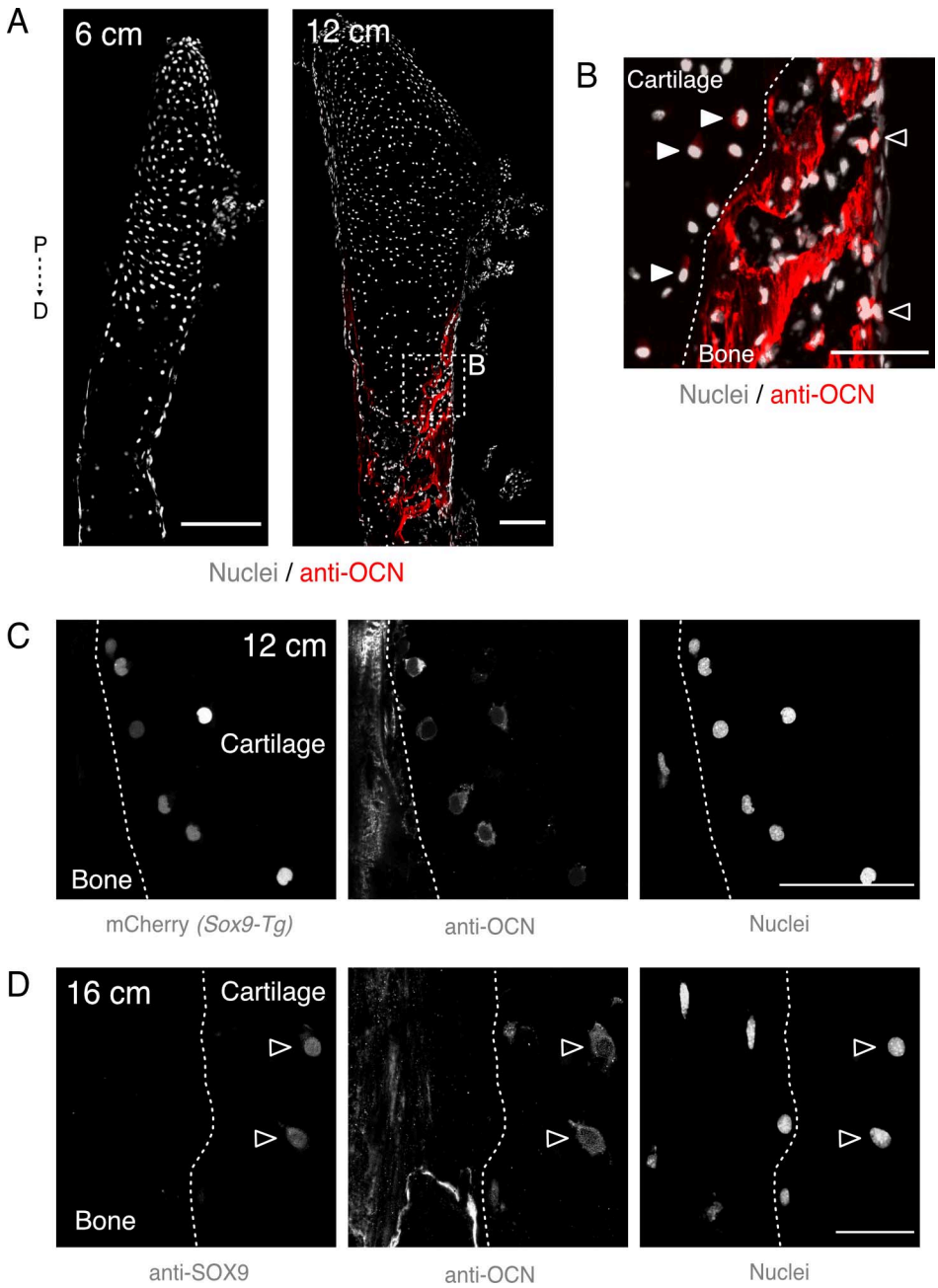
A
6 cm
12 cm
P
D
B
Nuclei / anti-OCN
B
Cartilage
Bone
Nuclei / anti-OCN
C
12 cm
Cartilage
Bone
mCherry (Sox9-Tg)
anti-OCN
Nuclei
D
16 cm
Cartilage
Bone
anti-SOX9
anti-OCN
Nuclei

1067

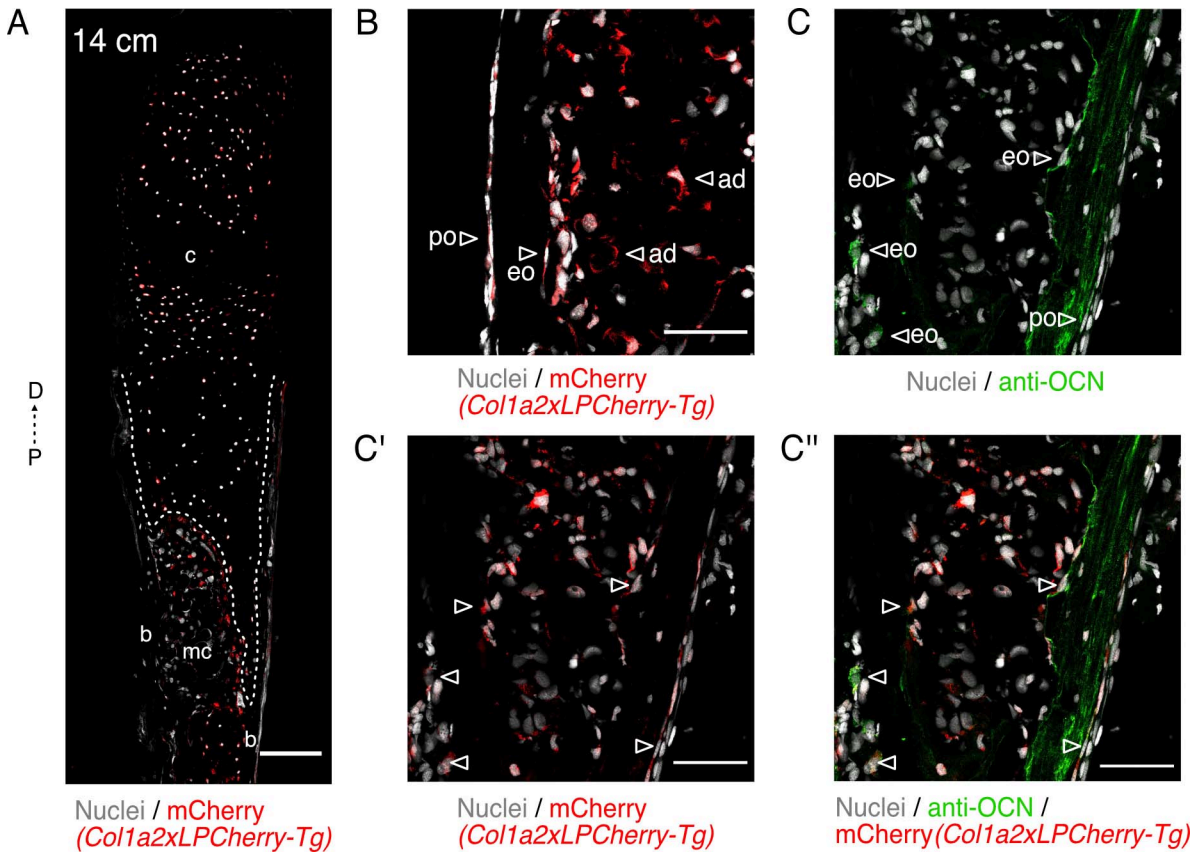
A
14 cm
c
D
P
b
mc
b
Nuclei / mCherry
(Col1a2xLPCherry-Tg)
B
po
eo
ad
ad
Nuclei / mCherry
(Col1a2xLPCherry-Tg)
C
eo
eo
eo
eo
po
Nuclei / anti-OCN
C'
Nuclei / mCherry
(Col1a2xLPCherry-Tg)
C''
Nuclei / anti-OCN /
mCherry(Col1a2xLPCherry-Tg)

1068

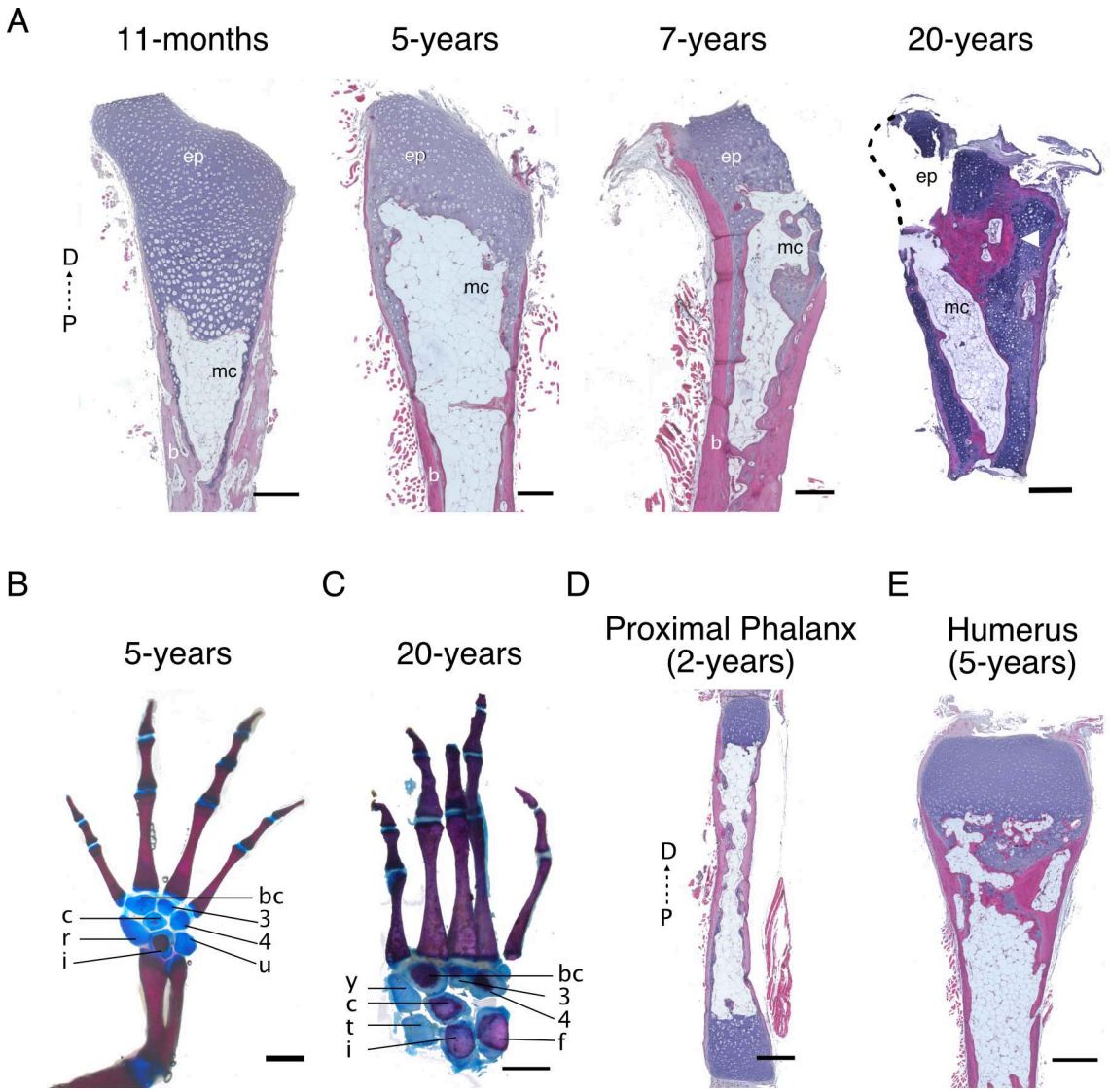
A
11-months
5-years
7-years
20-years
ep
mc
b
D
P
B
5-years
C
20-years
D
Proximal Phalanx
(2-years)
E
Humerus
(5-years)
bc
3
4
u
c
r
i
y
t
f

1069

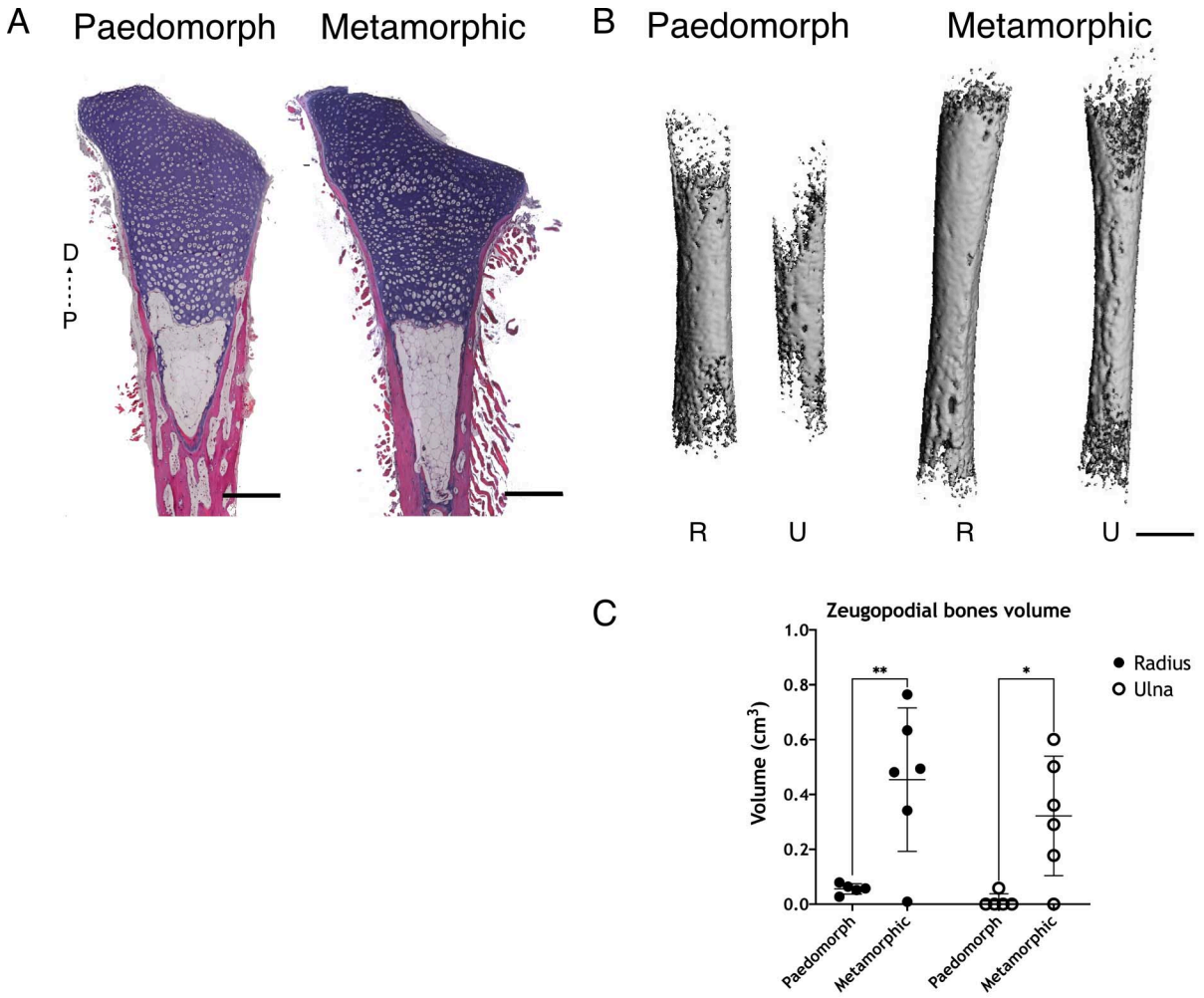

1070

1071

1072